

A Homoleptic Fe(IV) Ketimide Complex with a Low-Lying Excited State

Phoebe R. Hertler^a, Arturo Sauza-de la Vega^b, Andrea Darù^b, Arup Sarkar^b, Richard A. Lewis^a,
Guang Wu^a, Laura Gagliardi^{b*}, and Trevor W. Hayton^{a*}

^a*Department of Chemistry and Biochemistry, University of California Santa Barbara, Santa Barbara, CA 93106*

^b*Department of Chemistry, Pritzker School of Molecular Engineering, James Franck Institute, University of Chicago, Chicago, IL 60637*

*To whom correspondence should be addressed. Email: hayton@chem.ucsb.edu;
lgagliardi@uchicago.edu

Table of Contents

1. Experimental Details	S3
2. X-ray Crystallography Data Collection and Refinement Details	S8
3. NMR Spectra	S12
4. IR Spectra	S26
5. UV-vis/NIR Spectrum	S28
6. ^{57}Fe Mössbauer Spectrum	S29
7. Cyclic Voltammetry	S30
8. Magnetic Measurements	S34
9. Computational Details	S36
10. References	S58

Experimental Details

General Procedures. All operations were performed in a glovebox under an atmosphere of N₂. Diethyl ether (Et₂O) and hexanes were dried by passage over activated molecular sieves using a Vacuum Atmospheres DRI-SOLV solvent purification system. Tetrahydrofuran (THF) was first distilled from calcium hydride, then distilled from Na/benzophenone and stored over activated 3 Å molecular sieves for 24 h prior to use. Dimethoxyethane (DME) was distilled from Na/benzophenone and stored over activated 3 Å molecular sieves for 24 h prior to use. C₆D₆, toluene-*d*₈, THF-*d*₈, and PhCN were dried over activated 3 Å molecular sieves for 72 h prior to use. FeCl₂ was purchased from Strem and stirred in a mixture of Et₂O and TMSCl for 18 h at room temperature prior to use. Li(N=C(^tBu)Ph) was prepared according to published literature procedures.¹ All other reagents were purchased from commercial suppliers and used as received.

All NMR spectra were collected at room temperature unless otherwise specified. ¹H, ¹³C{¹H}, and ⁷Li{¹H} NMR spectra were recorded on an Agilent Technologies 400-MR DD2 400 MHz, a Varian Unity Inova 500 MHz spectrometer, a Bruker Avance NEO 500 MHz spectrometer, a Varian Unity Inova AS600 600 MHz spectrometer, or a Nanalysis 60e Single-Channel 60 MHz spectrometer. NMR spectra were referenced to external SiMe₄ using residual protio solvent resonances as internal standards. IR spectra were recorded on a Nicolet 6700 FT-IR spectrometer. Electronic absorption spectra were recorded on a PerkinElmer Lambda 750 UV/Vis/NIR Spectrophotometer. Elemental analyses were performed by the Microanalytical Laboratory at the University of California, Berkeley, using a Perkin Elmer 2400 Series II combustion analyzer.

Cyclic Voltammetry Measurements. CV experiments were performed with a CH Instruments 600c Potentiostat, and the data were processed using CHI software (version 6.29). All experiments were performed in a glovebox using a 20 mL glass vial as the cell. The working electrode consisted of a platinum disk embedded in glass (2 mm diameter), the counter electrode and the reference electrode were a platinum wire. Solutions employed for CV studies were 1 mM in analyte, and 0.1 M in [NBu₄][PF₆]. All potentials are reported versus the [Cp₂Fe]^{0/+} couple.

Zero-Field ⁵⁷Fe Mössbauer Spectroscopy. Data were collected on a SEECO Model W304 resonant gamma-ray spectrometer (activity = 50 mCi ± 10%), ⁵⁷Co/Rh source (manufactured by Ritverc) equipped with a Janis Research Model SVT-400 cryostat system. The source linewidth is <0.12 mm/s for the outermost lines of a 25 micron α -Fe foil standard. Isomer shifts are referenced to a α -Fe foil at room temperature. ⁵⁷Fe Mössbauer samples were prepared using crystalline material, suspended in Paratone-N oil. The samples were loaded into a polypropylene capsule under inert atmosphere, which was subsequently sealed with vacuum grease to prevent exposure to air. For the 90 K measurements, samples were prepared using 24 mg of crystalline **1**, and 24 mg of crystalline **2**. For the 298 K measurement, the sample was prepared using 116 mg of crystalline **2**. The data were fit using MossA, a custom Matlab package developed by the Prescher group at the University of Freiberg.²

Magnetism Measurements. Magnetic properties were recorded using a Quantum Design Magnetic Property Measurement System SQUID vibrating sample magnetometer (MPMS3 SQUID-VSM). A 35.0 mg sample of polycrystalline **2** was loaded into a quartz NMR tube, which was subsequently flame sealed under static vacuum. The solids were kept in place by quartz wool

packed on either side of the sample. DC magnetic measurements were performed in VSM mode while sweeping the temperature at controlled rates. For the magnetic susceptibility measurements, diamagnetic corrections ($\chi_{\text{dia}} = -4.34 \cdot 10^{-4} \text{ cm}^3/\text{mol}$ for $[\text{Fe}(\text{N}=\text{C}(\text{tBu})\text{Ph})_4]$) were made using Pascal's constants.³ The data were not corrected for the contribution from the sample holder and quartz wool.

Synthesis of $[\text{Li}(\text{Et}_2\text{O})_2][\text{Fe}(\text{N}=\text{C}(\text{tBu})\text{Ph})_4]$ (1). To a room temperature, orange, stirring suspension of $\text{LiN}=\text{C}(\text{tBu})\text{Ph}$ (452 mg, 2.70 mmol) in Et_2O (4 mL) was added FeCl_2 (87 mg, 0.69 mmol), which resulted in immediate color change to red-orange. THF (1.5 mL) was then added to the solution, resulting in dissolution of the undissolved solids. After 18 h of stirring, the solution darkened further to a deep red-orange, concomitant with deposition of a fine gray precipitate. The solution was then filtered through a Celite column supported on glass wool (0.5 cm · 3 cm). The filtrate was dried *in vacuo* and triturated with Et_2O (2 · 2 mL). The resulting dark red solid was extracted with a 4:1 solution of pentane and Et_2O (total volume: 6 mL), and filtered through a Celite column supported on glass wool (0.5 cm · 3 cm). The volume of the solution was reduced *in vacuo* to 2 mL. Storage of this solution at -25°C for 24 h resulted in the deposition of crystalline orange blocks, which were isolated by decanting off the supernatant and rinsing with cold pentane (3 mL, -25°C). 442 mg, 76% yield.

Elem. Anal. Found: C 72.74; H 8.83; N 6.64%. Calcd for $\text{C}_{52}\text{H}_{76}\text{FeN}_4\text{Li}_2\text{O}_2$: C 72.71; H 8.92; N 6.52%.

^1H NMR (THF- d_8 , 23°C , 400 MHz): δ 16.01 (br s, 9H, CMe_3), 12.67 (br s, 2H, Ph), 7.87 (br s, 2H, Ph). The *p*-Ph resonance was not observed, likely due to paramagnetic broadening.

^7Li NMR (THF- d_8 , 23°C , 155 MHz): δ 391 (br s).

FT-IR (KBr pellet, cm^{-1}): 455 (m), 575 (m), 702 (s), 773 (s), 791 (w), 850 (w), 899 (m), 943 (s), 960 (w), 1026 (w), 1072 (w), 1097 (w), 1101 (w), 1190 (m), 1360 (m), 1387 (w), 1441 (m), 1460 (m), 1477 (m), 1622 (s), 1803 (w), 1871 (w), 1942 (w).

Zero-field ^{57}Fe Mössbauer (90 K): $\delta = 0.924(2) \text{ mm/s}$, $|\Delta E_Q| = 3.537(4)$, $\Gamma = 0.410(7) \text{ mm/s}$.

Synthesis of $[\text{Fe}(\text{N}=\text{C}(\text{tBu})\text{Ph})_4]$ (2). To a chilled (-25°C), stirring, orange solution of **1** (139.7 mg, 0.16 mmol) in THF (3 mL) was slowly added dropwise a THF solution (2 mL) of I_2 (41 mg, 0.16 mmol). The solution immediately turned dark brown. After 20 min of stirring, the solution was dried *in vacuo* and the resulting black solid was dissolved in Et_2O (6 mL). The solution was filtered through a Celite column supported on glass wool (0.5 cm \times 3 cm), and the volume of the filtrate was reduced *in vacuo* to 3 mL. DME (0.5 mL) was then added to the solution. Storage of this solution at -25°C for 1 h resulted in the deposition of colorless needles, which were assumed to be $\text{LiI}(\text{DME})_2$. The solution was again filtered through a Celite column supported on glass wool (0.5 cm \times 3 cm), and the volume of the filtrate was reduced *in vacuo* to 2 mL. Further storage of this solution at -25°C for 24 h resulted in the deposition of more colorless crystals. The solution was again filtered through a Celite column supported on glass wool (0.5 cm \times 2 cm). The volume of the filtrate was reduced *in vacuo* to 1 mL and hexanes (0.5 mL) was layered onto the solution.

Storage of this solution at -25 °C for 24 h resulted in the deposition of black blocks, which were isolated by decanting the supernatant and rinsing with cold hexanes (2 mL). 36.5 mg, 32% yield.

Elem. Anal. Found: C 75.57; H 8.02; N 8.05%. Calcd for C₄₄H₅₆FeN₄: C 75.84; H 8.10; N 8.04%.

¹H NMR (C₆D₆, 23 °C, 600 MHz): δ 9.06 (s, 2H, *m*-Ph), 7.78 (br s, 2H, *o*-Ph), 5.28 (s, 1H, *p*-Ph), 2.81 (s, 9H, CMe₃).

¹H NMR (C₇D₈, 23 °C, 500 MHz): δ 8.92 (s, 2H, *m*-Ph), 7.70 (s, 2H, *o*-Ph), 5.33 (s, 1H, *p*-Ph), 2.68 (s, 9H, CMe₃).

¹H NMR (C₇D₈, 0 °C, 500 MHz): δ 8.38 (s, 2H, *m*-Ph), 7.52 (s, 2H, *o*-Ph), 5.72 (s, 1H, *p*-Ph), 2.30 (s, 9H, CMe₃).

¹H NMR (C₇D₈, -20 °C, 500 MHz): δ 7.97 (s, 2H, *m*-Ph), 7.37 (s, 2H, *o*-Ph), 6.01 (s, 1H, *p*-Ph), 2.04 (s, 9H, CMe₃).

¹H NMR (C₇D₈, -40 °C, 500 MHz): δ 7.62 (s, 2H, *m*-Ph), 7.27 (s, 2H, *o*-Ph), 6.26 (s, 1H, *p*-Ph), 1.84 (s, 9H, CMe₃).

¹H NMR (C₇D₈, -60 °C, 500 MHz): δ 7.37 (s, 2H, *m*-Ph), 7.09 (s, 2H, *o*-Ph), 6.42 (s, 1H, *p*-Ph), 1.71 (s, 9H, CMe₃).

¹³C{¹H} NMR (C₆D₆, 23 °C, 125 MHz): δ 157.07 (s, *p*-Ph), 136.47 (s, *o*- or *m*-Ph), 131.97 (s, *o*- or *m*-Ph), 50.36 (s, Me). The *ipso*-C, CMe₃, and C=N carbon resonances were not observed, likely due to paramagnetic broadening.

¹H NMR (C₆D₆, 23 °C, 60 MHz): δ 9.25 (s, 2H, *m*-Ph), 5.15 (s, 1H, *p*-Ph), 2.95 (s, 9H, CMe₃). The *o*-Ph resonance was not observed, likely due to paramagnetic broadening and poor spectral resolution.

FT-IR (KBr pellet, cm⁻¹): 496 (s), 552 (m), 640 (m), 696 (s), 727 (m), 773 (m), 818 (w), 839 (w), 933 (m), 945 (s), 1001 (w), 1026 (m), 1072 (w), 1188 (s), 1201 (m), 1275 (w), 1360 (s), 1354 (m), 1441 (m), 1443 (m), 1473 (m), 1481 (m), 1578 (w), 1595 (m), 1676 (m), 2343 (w), 2360 (w).

UV-vis/NIR (pentane, 0.1 mM, 25 °C, L mol⁻¹ cm⁻¹): 307 nm (ε = 17683), 469 nm (ε = 25068), 574 nm (ε = 4448), 739 nm (ε = 6883), 910 nm (ε = 2971).

Zero-field ⁵⁷Fe Mössbauer (90 K): δ = -0.162(2) mm/s, |ΔE_Q| = 1.837(3) mm/s, Γ = 0.296(5) mm/s.

Zero-field ⁵⁷Fe Mössbauer (298 K): δ = -0.096(4) mm/s, |ΔE_Q| = 1.172(7) mm/s, Γ = 0.220 mm/s.

Oxidation of 1 with AgPF₆. To a chilled (-25 °C), stirring, orange solution of **1** (94.3 mg, 0.11 mmol) in Et₂O (4 mL) was added AgPF₆ (47.0 mg, 0.19 mmol, 1.7 equiv) as a solid. The solution immediately turned dark brown. After 10 min of stirring at 23 °C, an aliquot (0.5 mL) was removed from the reaction mixture and dried *in vacuo*. The resulting solid was redissolved in C₆D₆ (0.5

mL) and filtered through a Celite column supported on glass wool (0.5 cm × 2 cm) into an NMR tube. A ¹H NMR spectrum revealed the presence of **2** and **3**, along with several unassigned decomposition products (**Figure S11**).

¹H NMR (C₆D₆, 23 °C, 500 MHz): δ 35.8 (br s, unassigned), 27.0 (br s, unassigned), 22.6 (br s, unassigned), 18.2 (br s, **3**, *o*- or *m*-Ph), 16.4 (br s, **3**, Me), 12.8 (br s, **3**, *o*- or *m*-Ph), 9.06 (s, **2**, *m*-Ph), 7.73 (br s, **2**, *o*-Ph), 7.01 (s, unassigned), 5.26 (s, **2**, *p*-Ph), 3.26 (s, Et₂O), 2.80 (s, **2**, CMe₃), 1.12 (s, Et₂O), 1.03 (s, unassigned).

Oxidation of 1 with [Cp₂Fe][BF₄]. To a chilled (-25 °C), stirring, orange solution of **1** (119.8 mg, 0.14 mmol) in Et₂O (3.5 mL) was added [Cp₂Fe][BF₄] (66.0 mg, 0.24 mmol, 1.7 equiv) as a solid. The solution immediately turned dark brown. After 15 min of stirring at 23 °C, an aliquot (0.5 mL) was removed from the reaction mixture and dried *in vacuo*. The resulting solid was redissolved in C₆D₆ (0.5 mL) and filtered through a Celite column supported on glass wool (0.5 cm × 2 cm) into an NMR tube, A ¹H NMR spectrum revealed the formation of **2** and Cp₂Fe in the reaction mixture (**Figure S12**). Attempts to separate **2** from Cp₂Fe proved too challenging due to their similar solubility.

¹H NMR (C₆D₆, 23 °C, 500 MHz): δ 9.87 (br s, unassigned), 9.23 (br s, NH, HN=C(^tBu)Ph), 9.06 (s, **2**, *m*-Ph), 7.78 (br s, **2**, *o*-Ph), 7.41 (s, unassigned), 7.32 (s, unassigned), 7.01 (m, *p*- and *o*-Ar, HN=C(^tBu)Ph), 6.89 (m, *m*-Ar, HN=C(^tBu)Ph), 5.27 (s, **2**, *p*-Ph), 4.01 (s, [Cp₂Fe]), 3.26 (q, Et₂O), 2.81 (s, **2**, CMe₃), 1.24 (s, CMe₃, HN=C(^tBu)Ph), 1.12 (t, Et₂O), 1.01 (s, unassigned), 0.90 (s, hexanes), 0.30 (s, unassigned).

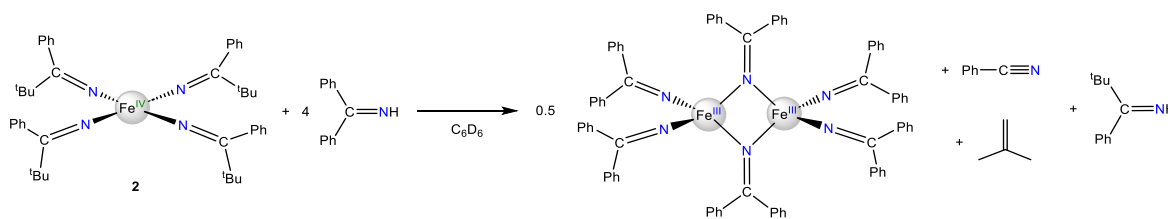
Thermolysis of Complex 2. A deep brown solution of **2** (13 mg, 0.02 mmol) in C₆D₆ (0.5 mL) was added to a J-young NMR tube. The tube was sealed, removed from the glovebox, and the solution was heated to 50 °C for 3 h, which resulted in a color change to deep purple. ¹H and ¹³C{¹H} NMR spectra were then recorded (**Figures S13-S14**), which revealed the absence of resonances assignable to **2**, along with appearance of resonances assignable to [Fe₂(N=C(^tBu)Ph)₆] (**3**),⁴ PhCN,⁵ isobutylene,^{6,7} and HN=C(^tBu)Ph.^{8,9}

¹H NMR (C₆D₆, 23 °C, 500 MHz): δ 19.27 (br s, **3**, Me), 18.16 (br s, **3**, *o*- or *m*-Ph), 16.40 (br s, **3**, Me), 12.79 (br s, **3**, *o*- or *m*-Ph), 9.11 (br s, NH, HN=C(^tBu)Ph), 7.01 (br s, *p*- and *o*-Ar, HN=C(^tBu)Ph), 6.96 (d, *J*_{HH} = 7.0 Hz, *o*-Ar, PhCN), 6.88 (br s, *m*-Ar, HN=C(^tBu)Ph), 6.79 (t, *J*_{HH} = 7.5 Hz, *p*-Ar, PhCN), 6.63 (t, *J*_{HH} = 7.5 Hz, *m*-Ar, PhCN), 4.75 (s, CH₂, isobutylene), 2.48 (br s, **3**, *p*-Ph), 1.61 (s, unidentified), 1.60 (s, CMe₂, isobutylene), 1.35 (br s, **3**, *o*- or *m*-Ph), 1.23 (br s, CMe₃, HN=C(^tBu)Ph), 1.18 (s, unidentified), 1.01 (s, unidentified).

¹³C{¹H} NMR (C₆D₆, 23 °C, 125 MHz): δ 257.20 (br s, **3**, *o*- or *m*-Ph), 244.36 (br s, **3**, *o*- or *m*-Ph), 188.88 (s, C=NH, HN=C(^tBu)Ph), 181.74 (br s, **3**, Me), 160.02 (br s, **3**, *p*-Ph), 151.84 (s, **3**, *o*- or *m*-Ph), 150.70 (s, **3**, *o*- or *m*-Ph), 144.38 (br s, **3**, CMe₃), 143.47 (s, *i*-C, HN=C(^tBu)Ph), 141.90 (s, C(Me)₂ isobutylene), 131.99 (s, *p*-C, PhCN), 118.80 (s, C≡N PhCN), 116.52 (br s, **3**, Me), 113.14 (s, *i*-C, PhCN), 111.26 (s, CH₂, isobutylene), 40.02 (s, CMe₃, HN=C(^tBu)Ph), 29.11 (s, CH₃, HN=C(^tBu)Ph), 24.14 (s, CH₃, isobutylene).

Reaction of Complex **2 with HN=CPh₂.** To a dark brown solution of **2** (7.8 mg, 0.011 mmol) in C₆D₆ (0.5 mL) in an NMR tube was added a solution of HN=CPh₂ (8.5 mg, 0.047 mmol) in C₆D₆ (0.5 mL). After 25 min, a ¹H NMR spectrum was recorded (**Figure S15**), which revealed the formation of Fe₂(N=CPh₂)₆,⁴ along with the appearance of resonances assignable to PhCN, isobutylene, and HN=C(^tBu)Ph, in addition to some unreacted **2** and HN=CPh₂.¹⁰

¹H NMR (C₆D₆, 23 °C, 400 MHz): δ 19.49 (br s, Fe₂(N=CPh₂)₆, *m*-Ph), 13.48 (br s, Fe₂(N=CPh₂)₆, *m*-Ph), 9.83 (br s, NH, HN=CPh₂), 9.23 (br s, NH, HN=C(^tBu)Ph), 9.07 (br s, *m*-Ar, **2**), 7.92 (br s), 7.12 (br s, *p*-Ar, HN=CPh₂), 7.05 (br s, *m*-Ar, NH=CPh₂), 7.01 (m, *p*- and *o*-Ar, HN=C(^tBu)Ph), 6.89 (d, *m*-Ar, *J*_{HH} = 4.4 Hz, HN=C(^tBu)Ph), 6.80 (t, *p*-Ar, *J*_{HH} = 6.4 Hz, PhCN), 6.64 (t, *m*-Ar, *J*_{HH} = 6 Hz, PhCN), 5.27 (s, *p*-Ar, **2**), 4.75 (s, CH₂, isobutylene), 2.82 (s, CMe₃, **2**), 1.61 (s, unidentified), 1.60 (s, CMe₂, isobutylene), 1.24 (s, CMe₃, HN=C(^tBu)Ph), 1.18 (s, unidentified), 1.01 (s, unidentified), -0.33 (br s, Fe₂(N=CPh₂)₆, *p*-Ph), -4.30 (br s, Fe₂(N=CPh₂)₆, *p*-Ph).



Scheme S1. Reaction of **2** with 4 equiv of HN=CPh₂.

X-ray Crystallography Data Collection and Refinement Details

Data for **1** and **2** were collected on a Bruker KAPPA APEX II diffractometer equipped with an APEX II CCD detector using a TRIUMPH monochromator with a Mo K α X-ray source ($\alpha = 0.71073 \text{ \AA}$). Crystals of **1** and **2** were mounted on a cryoloop under Paratone-N oil, and the data were collected at 100(2) K using an Oxford nitrogen gas cryostream system. The data for **2** were also collected at 287(2) K under the same conditions. X-ray data for **1** and **2** measured at 100 K were collected using frame exposures of 15 s and 20 s, respectively, and X-ray data for **2** measured at 287 K were collected using frame exposures of 20 s. Data collection and cell parameter determination were conducted using the SMART program.¹¹ Integration of the data frames and final cell parameter refinement were performed using SAINT software.¹² Absorption correction of the data was carried out using the multi-scan method SADABS.¹³ Subsequent calculations were carried out using SHELXTL.¹⁴ Structure determination was done using direct methods and difference Fourier techniques. All hydrogen atom positions were idealized and rode on the atom attachment. Structure solution, refinement, graphics, and creation of publication materials were performed using SHELXTL.¹⁴

For complex **1**, four carbons of one of the *tert*-butyl groups were constrained with the EADP command. Further crystallographic details can be found in **Table S1**. Complexes **1** and **2** have been deposited in the Cambridge Structural Database (**1**: CCDC 2254712; **2** (100 K): 2254713; **2** (287 K): 2363649).

Table S1. X-ray Crystallographic Data for **1** and **2**

	1	2 (100 K)	2 (287 K)
empirical formula	FeN ₄ C ₅₂ H ₇₆ Li ₂ O ₂	FeN ₄ C ₄₄ H ₅₆	FeN ₄ C ₄₄ H ₅₆
crystal habit, color	Block, yellow	Block, black	Block, black
crystal size (mm)	0.3×0.3 ×0.3	0.7×0.5×0.3	0.7×0.5×0.3
crystal system	Monoclinic	Monoclinic	Monoclinic
space group	P2 ₁ /c	C2/c	C2/c
volume (Å ³)	5521(3)	4021(2)	4255(5)
<i>a</i> (Å)	19.334(5)	23.042(6)	23.477(12)
<i>b</i> (Å)	13.388(4)	9.565(3)	9.781(5)
<i>c</i> (Å)	23.028(9)	21.412(8)	21.869(16)
α (deg)	90	90	90
β (deg)	112.142(3)	121.565(5)	122.075(8)
γ (deg)	90	90	90
Z	4	4	4
formula weight (g/mol)	858.89	696.77	696.77
density (calculated) (Mg/m ³)	1.033	1.151	1.088
absorption coefficient (mm ⁻¹)	0.310	0.409	0.386
F ₀₀₀	1856	1496	1496
total no. reflections	39849	13078	13888
unique reflections	9402	4131	4352
final R indices [<i>I</i> > 2σ(<i>I</i>)]	R ₁ = 0.0776 wR ₂ = 0.1998	R ₁ = 0.0441 wR ₂ = 0.0565	R ₁ = 0.0581 wR ₂ = 0.1466
largest diff. peak and hole (e ⁻ Å ⁻³)	1.193 and -1.166	0.540 and -0.506	0.347and -0.941
GOF	1.017	1.381	1.021

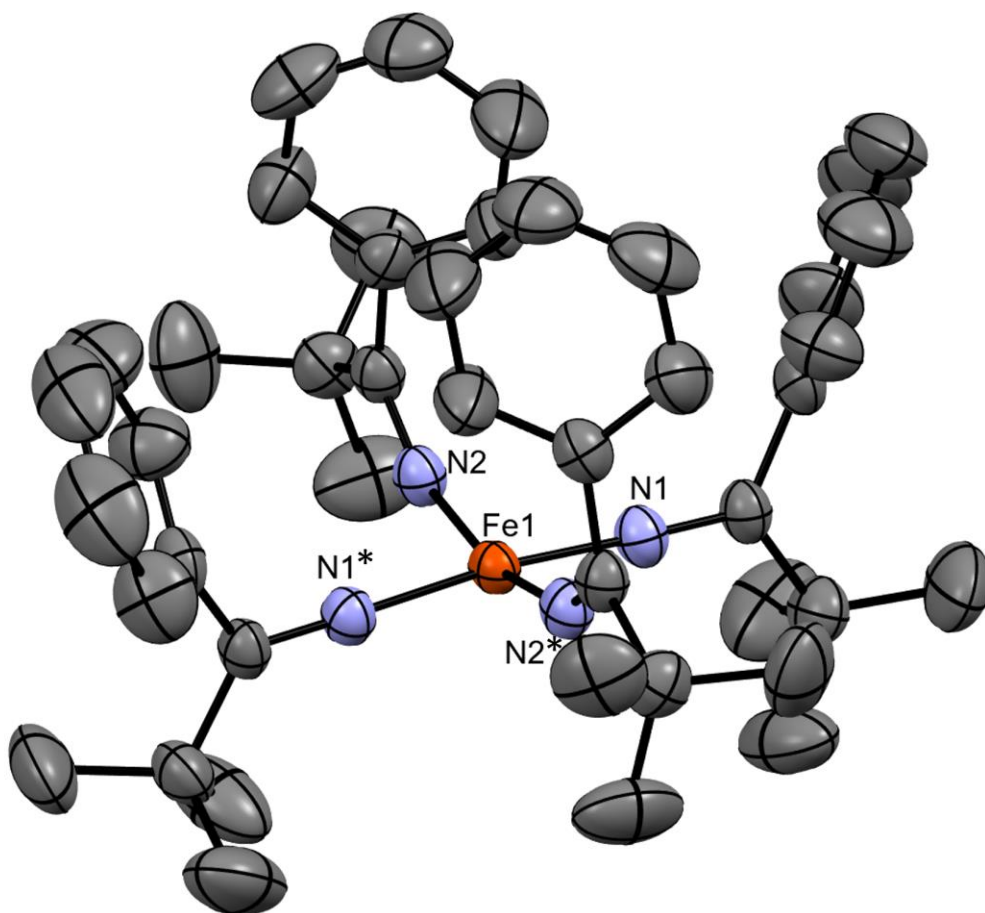


Figure S1. Solid-state structure of [Fe(N=(^tBu)Ph)₄] (**2**) with 50% probability ellipsoids, measured at 287 K. Hydrogen atoms are omitted for clarity.

Table S2. Metrical Comparisons between 100 K and 287 K Solid-State Structures of **2** (Å, °)

	100 K	287 K
Fe1–N1	1.7571(17)	1.763(2)
Fe1–N2	1.7859(15)	1.789(2)
N1–C1	1.253(2)	1.256(3)
N2–C12	1.256(2)	1.259(3)
N1–Fe1–N2	90.26(7)	90.33(9)
N1–Fe1–N2*	90.99(7)	90.88(10)
N1–Fe1–N1*	172.96(10)	172.90(12)
N2–Fe1–N2*	159.70(10)	160.37(12)
Fe–N1–C1	177.62(16)	178.54(18)
Fe–N2–C12	149.24(14)	150.71(19)
χ^2	0.19	0.19

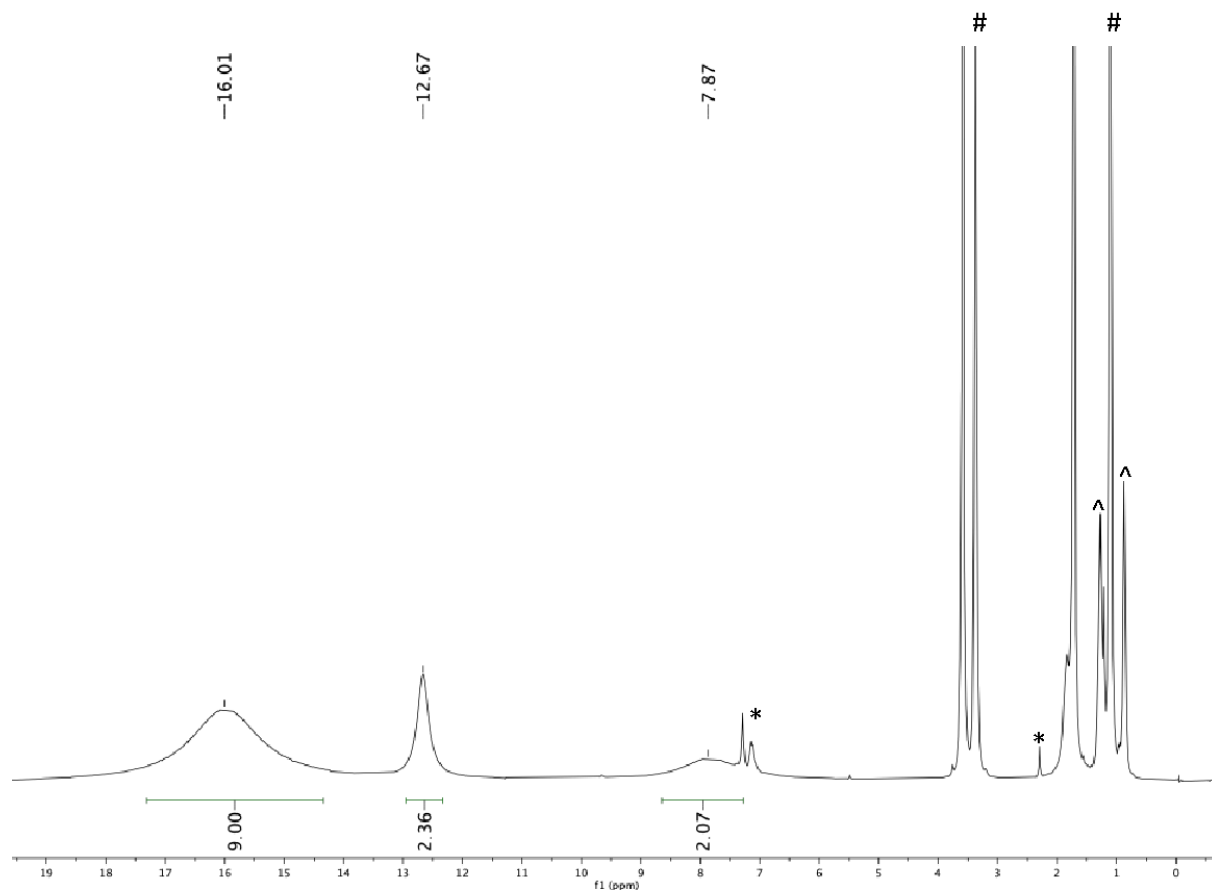


Figure S2. Room temperature ^1H NMR spectrum of **1** in $\text{THF-}d_8$. (#) indicates resonances assignable to free Et_2O , (^) indicates resonances assignable to hexanes, and (*) indicates resonances assignable to toluene.

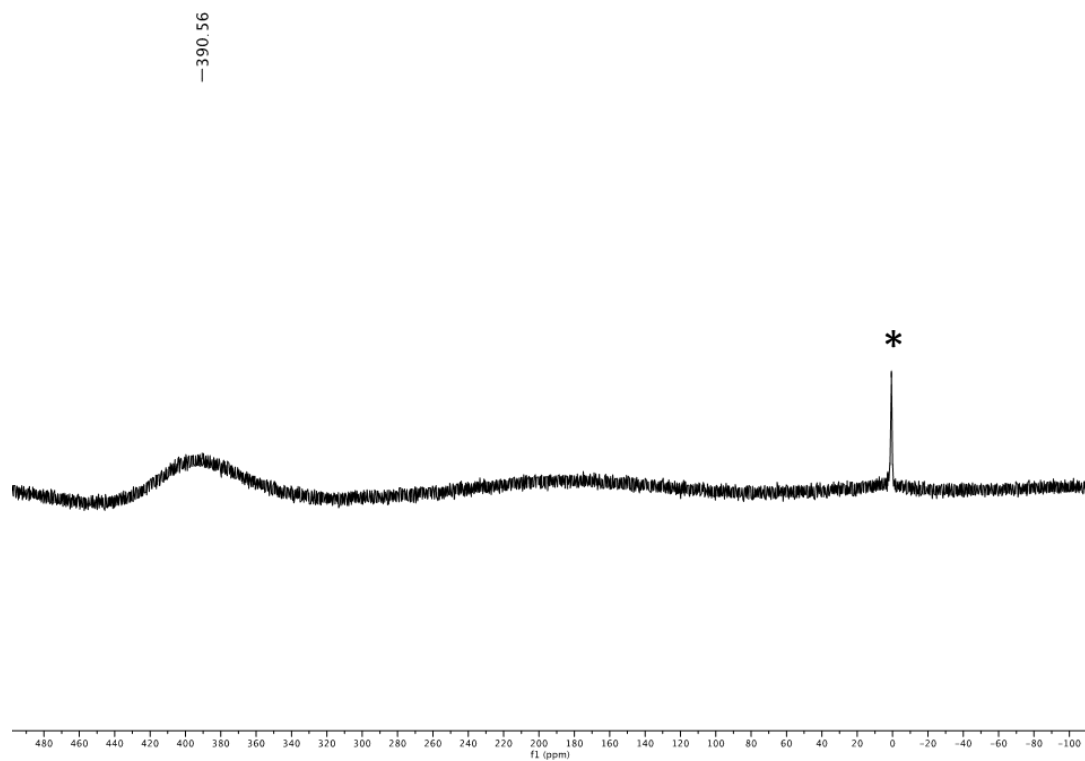


Figure S3. Room temperature ${}^7\text{Li}$ NMR spectrum of **1** in $\text{THF-}d_8$. (*) indicates a resonance that is assignable to a decomposition product of **1**.

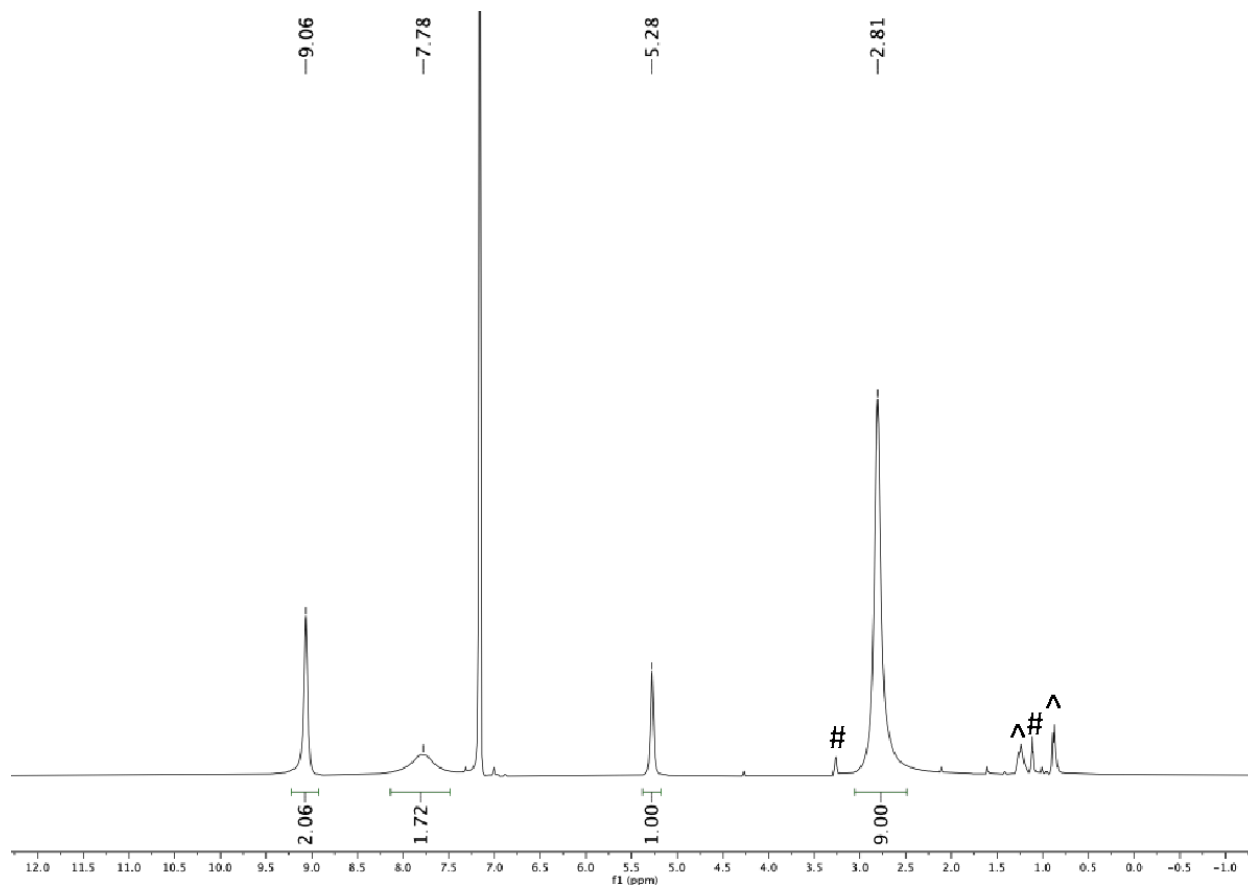


Figure S4. Room temperature ¹H NMR spectrum of **2** in C₆D₆. (#) indicates resonances assignable to Et₂O and (^) indicates resonances assignable to hexanes.

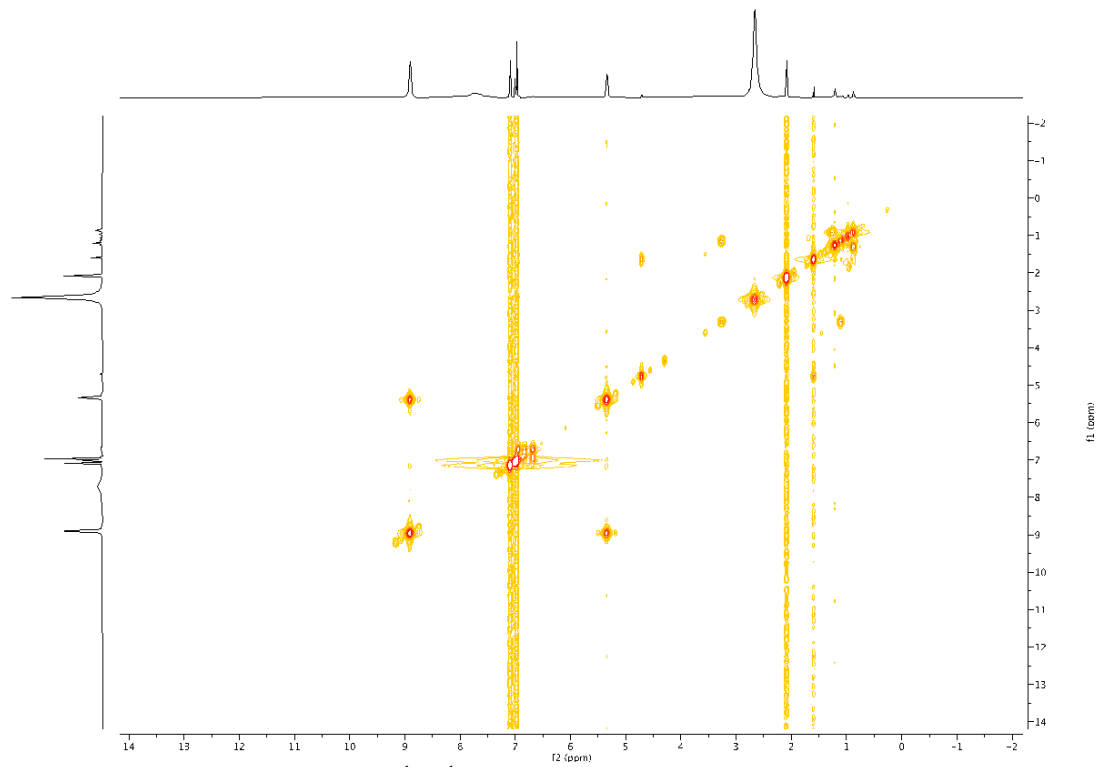


Figure S5. Room temperature ¹H-¹H COSY NMR spectrum of **2** in toluene-*d*₈.

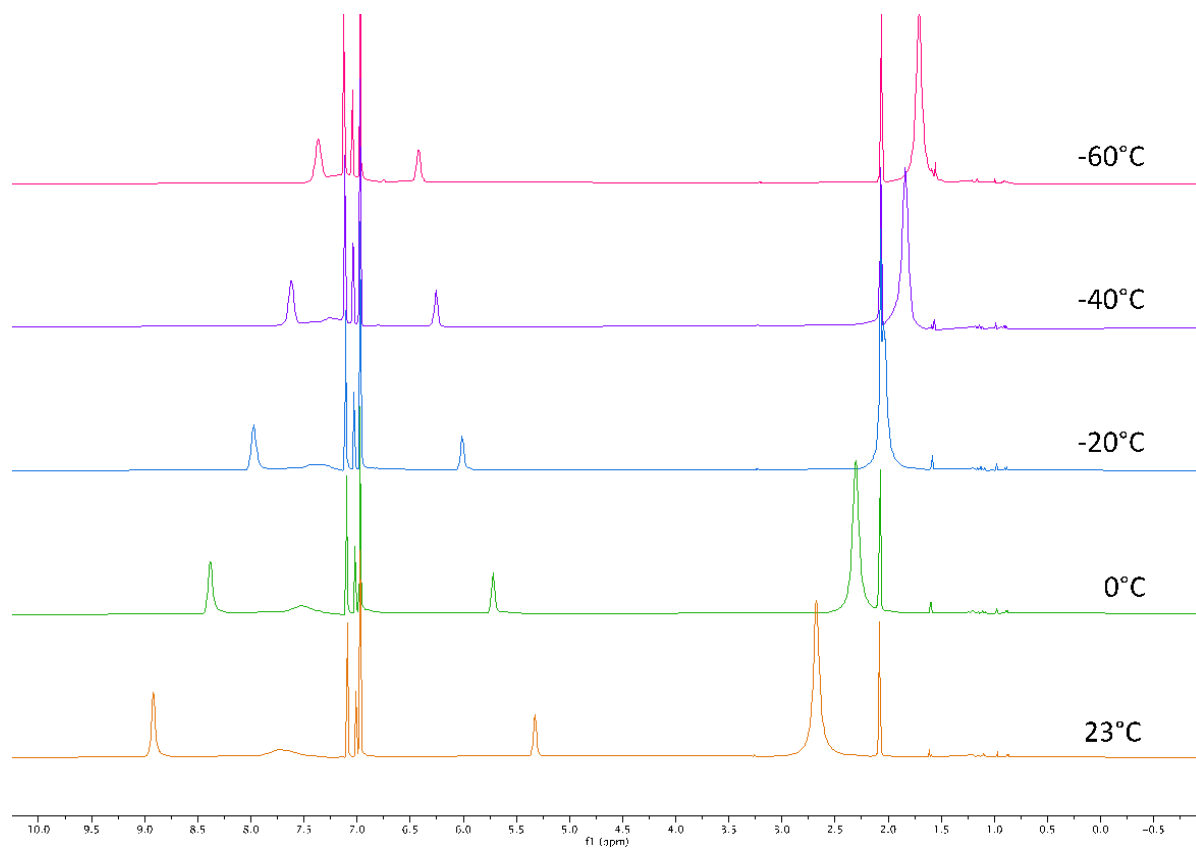


Figure S6. Variable temperature ¹H NMR spectrum of **2** in toluene-*d*₈.

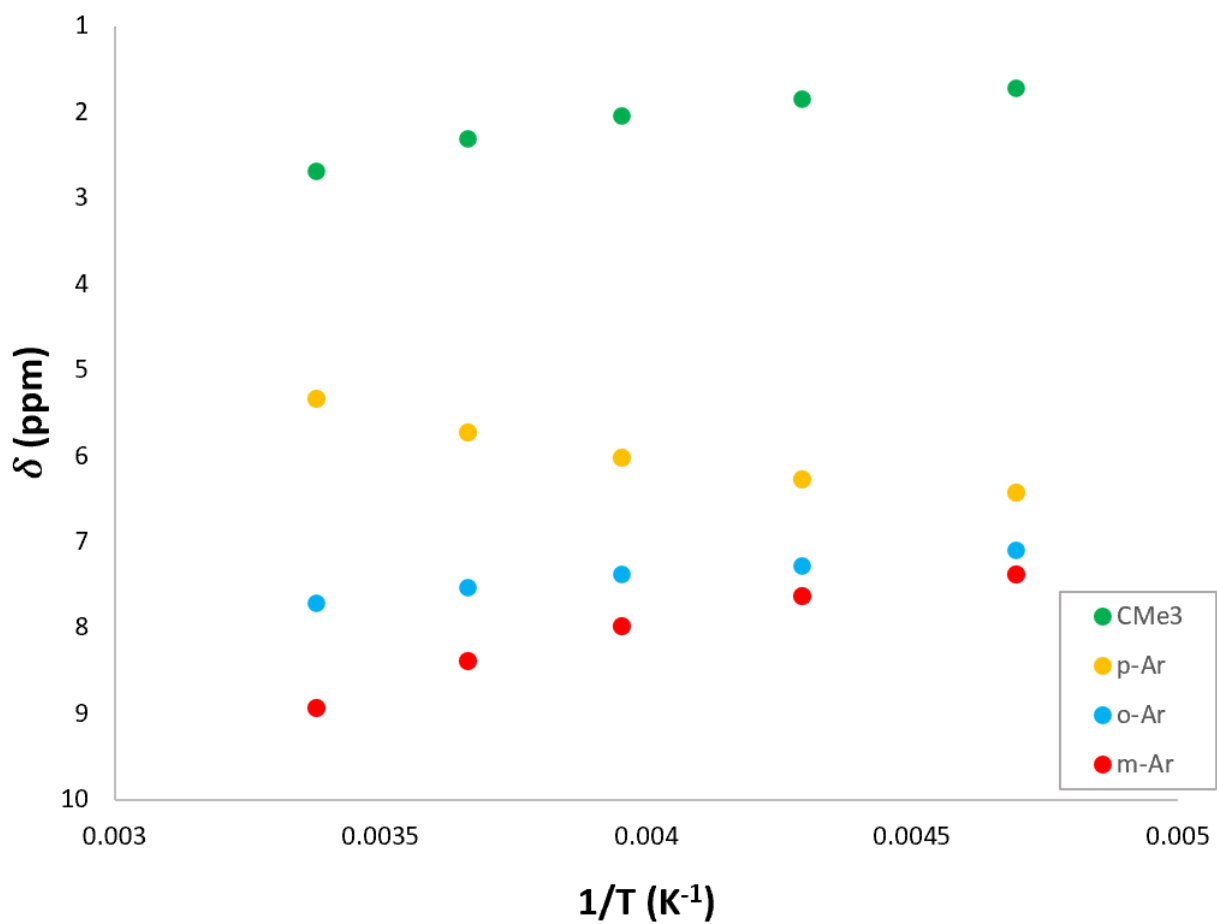


Figure S7. Plot of chemical shift versus K^{-1} of the variable temperature 1H NMR data of **2** in toluene- d_8 .

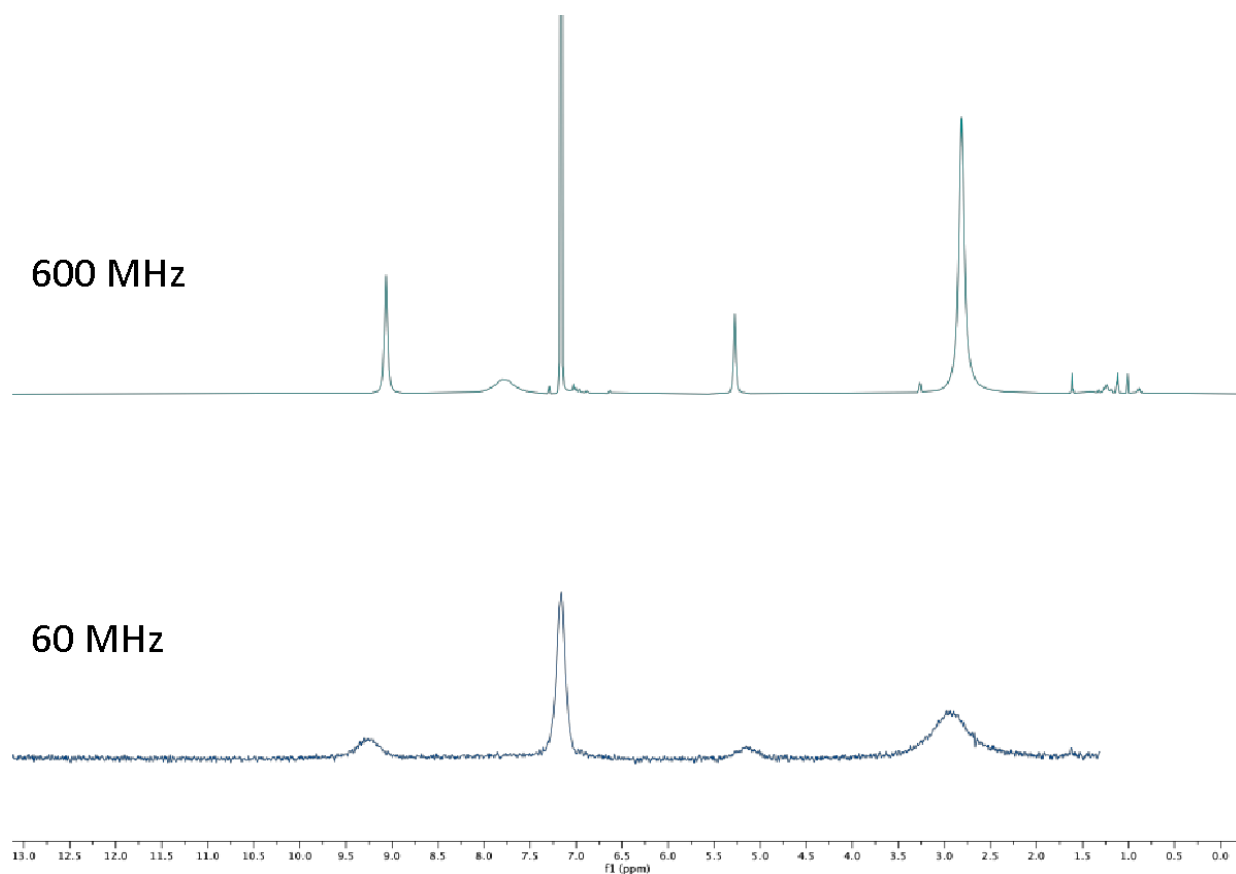


Figure S8. Room temperature ^1H NMR spectra in C_6D_6 of **2** recorded on a 600 MHz NMR spectrometer (top) and a 60 MHz NMR spectrometer (bottom).

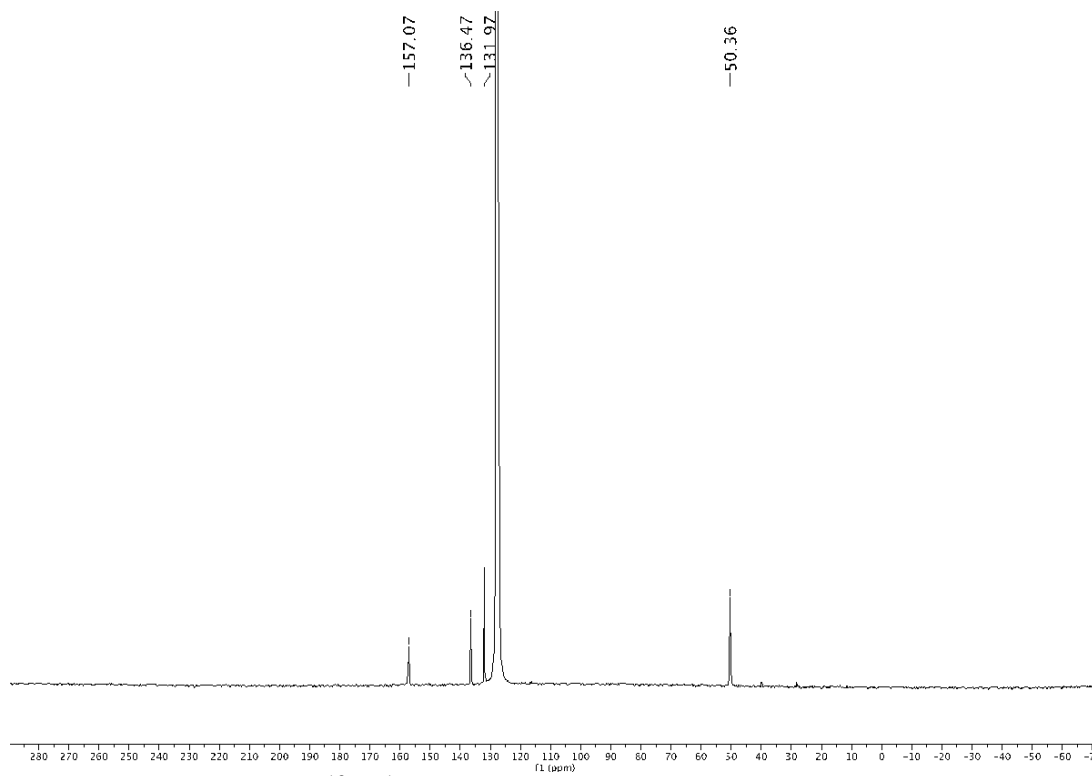


Figure S9. Room temperature $^{13}\text{C}\{^1\text{H}\}$ NMR spectrum of **2** in C_6D_6 .

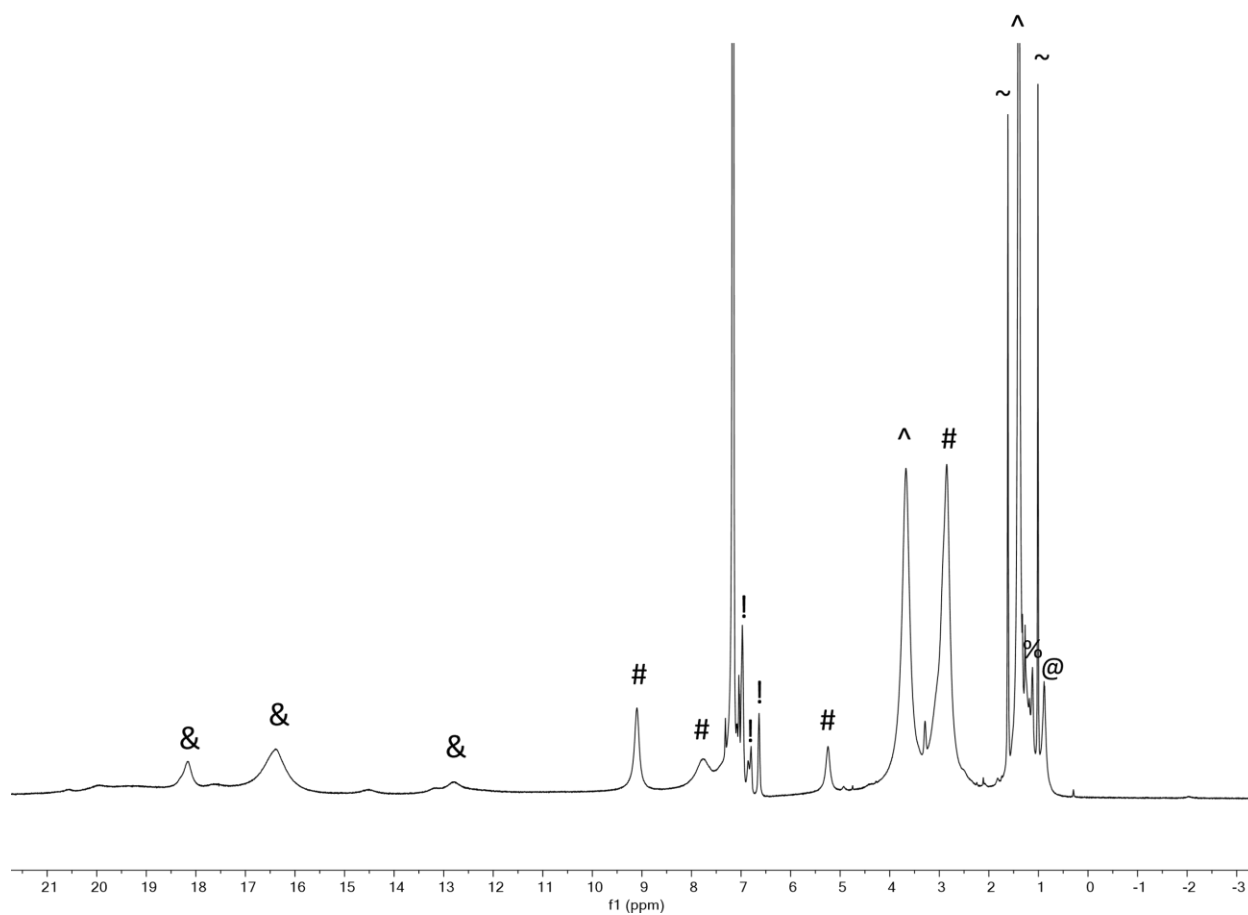


Figure S10. Room temperature ^1H NMR spectrum (in C_6D_6) of the crude reaction mixture formed after adding 1 equiv of I_2 to **1**. (#) indicates resonances assigned to **2**, and (&) indicates resonances assigned to **3**. (!) indicates resonances assigned to benzonitrile. (^) indicates resonances assigned to THF. (@) indicates resonances assignable to hexanes. (%) indicates resonances assignable to diethyl ether. (~) indicates resonances assigned to unidentified product(s).

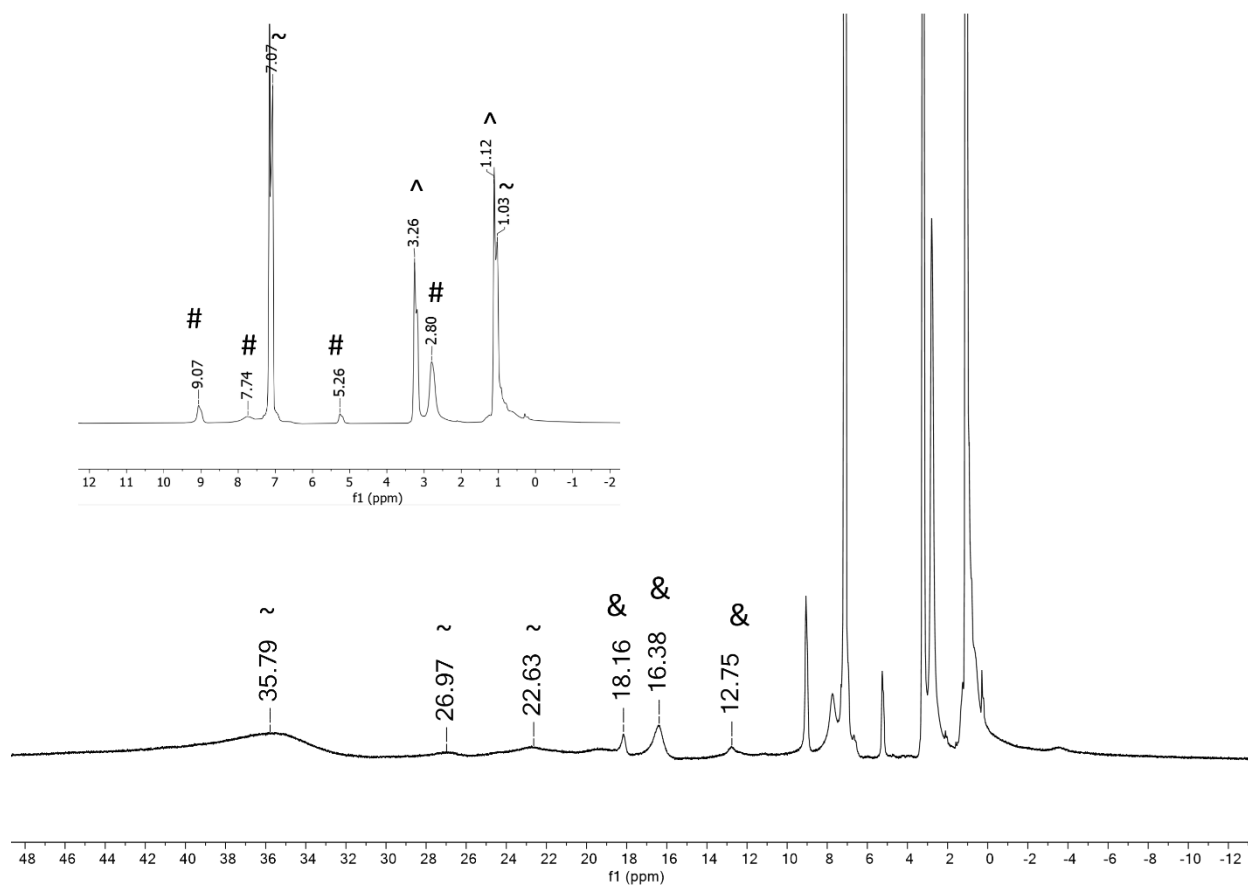


Figure S11. Room temperature ^1H NMR spectrum (in C_6D_6) of the crude reaction mixture formed after adding 1.7 equiv of AgPF_6 to **1**. (#) indicates resonances assigned to **2**, (&) indicates resonances assigned to **3**, (^) indicates resonances assigned to Et_2O , and (~) indicates resonances assigned to unidentified product(s).

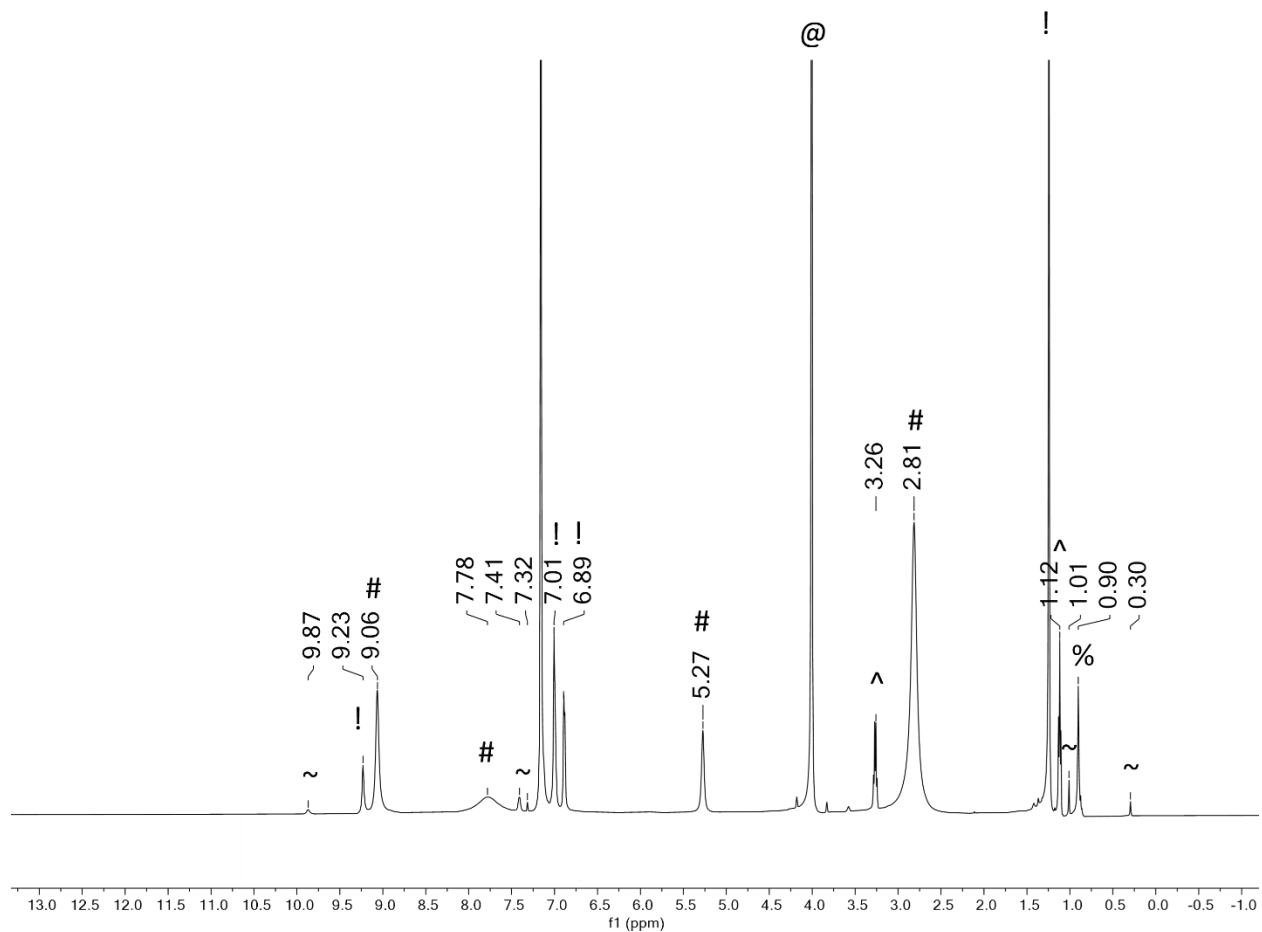


Figure S12. Room temperature ¹H NMR spectrum (in C₆D₆) of the crude reaction mixture formed after adding 1.7 equiv of [Cp₂Fe][BF₄] to **1**. (#) indicates resonances assigned to **2**, (!) indicates resonances assigned to HN=C(^tBu)Ph, (@) indicates resonances assigned to [Cp₂Fe], (^) indicates resonances assigned to Et₂O, (%) indicates resonances assigned to hexanes, and (~) indicates resonances assigned to unidentified product(s).

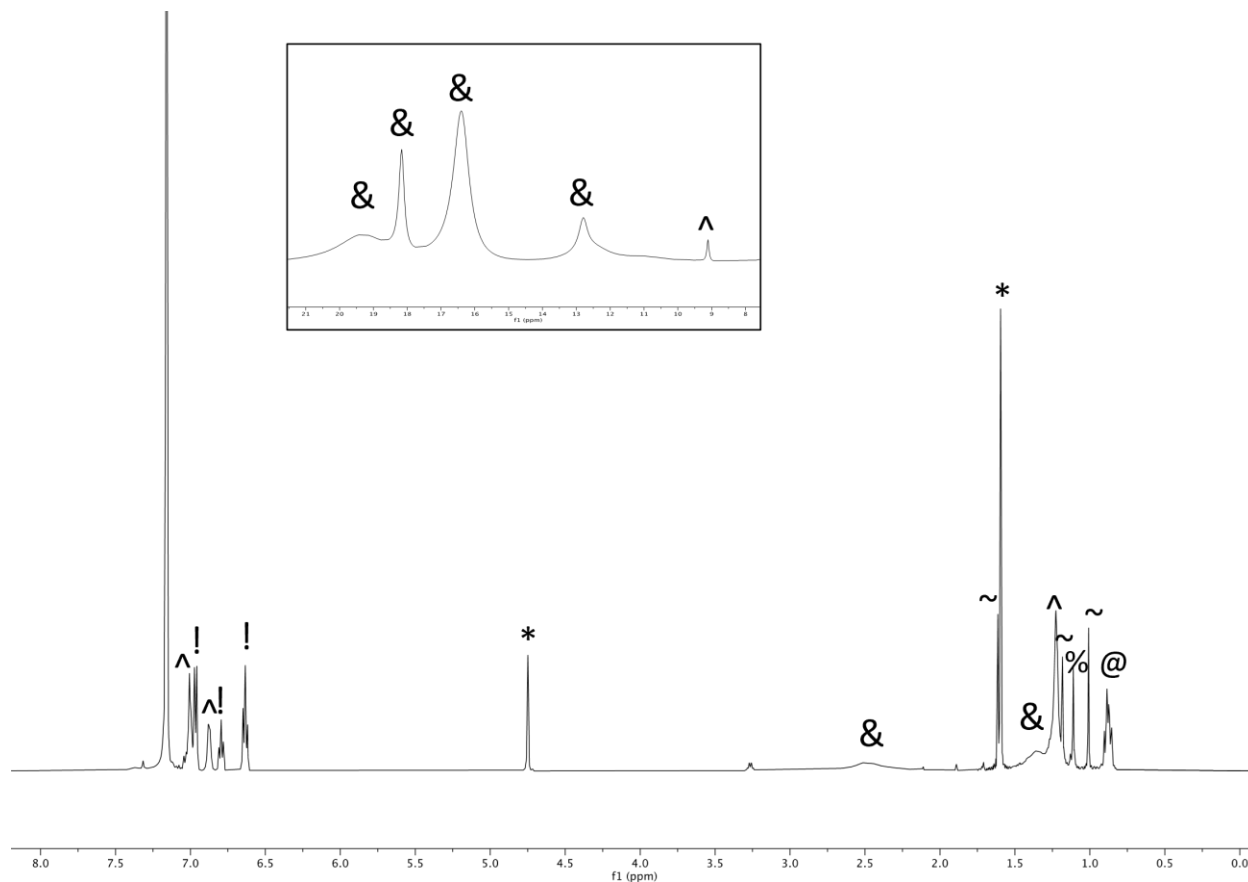


Figure S13. Room temperature ^1H NMR spectrum of complex **2** in C_6D_6 after 3 h of thermolysis at $50\text{ }^\circ\text{C}$. (*) indicates resonances assignable to vinyl and methyl protons of isobutylene. (!) indicates resonances assignable to benzonitrile. The inset contains the downfield region. (&) indicates resonances assignable to **3**. (^) indicates resonances assignable to $\text{HN}=\text{C}(\text{tBu})\text{Ph}$. (@) indicates resonances assignable to hexanes. (%) indicates resonances assignable to diethyl ether. (~) indicates resonances assigned to unidentified products.

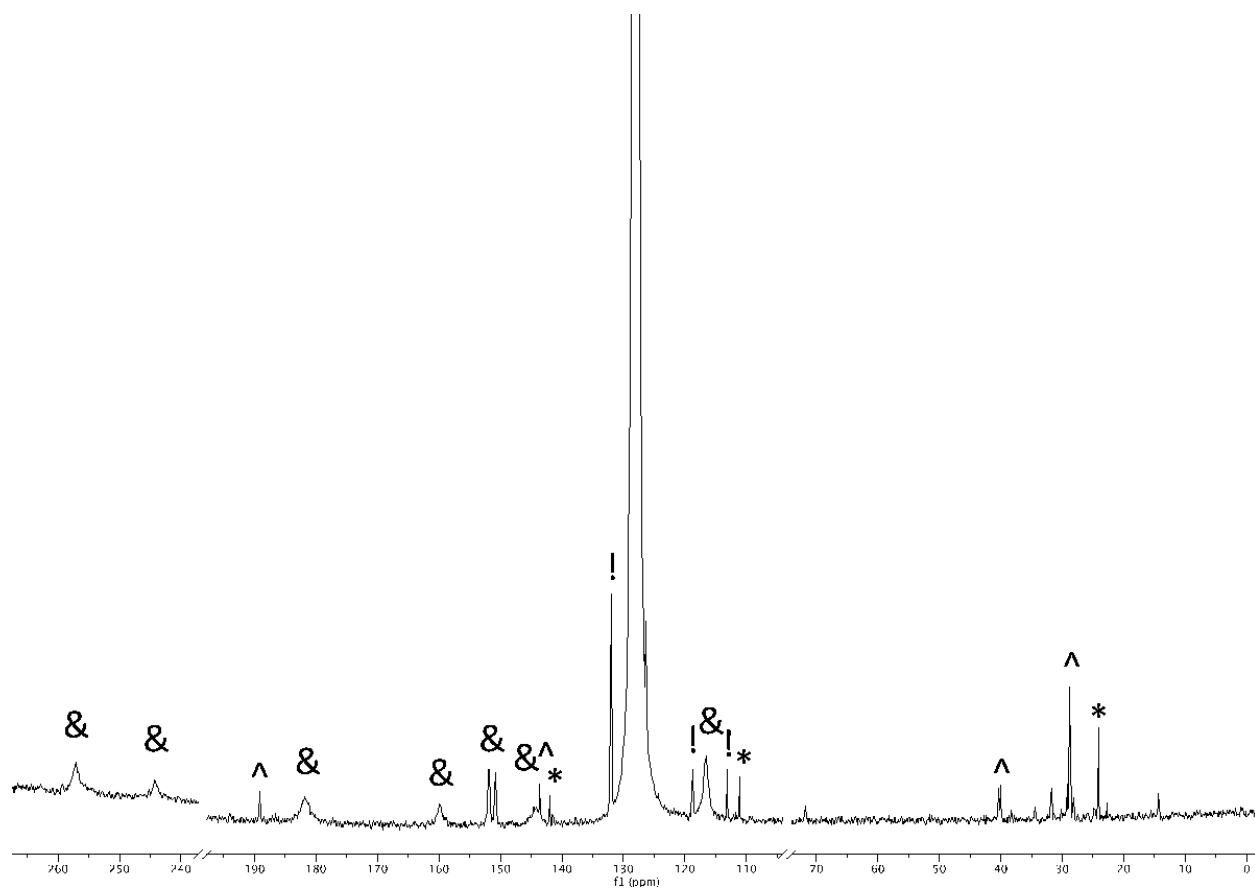


Figure S14. Room temperature $^{13}\text{C}\{^1\text{H}\}$ NMR spectrum of complex **2** in C_6D_6 after 3 h of thermolysis at $50\text{ }^\circ\text{C}$. (*) indicates resonances assignable to vinyl and methyl protons of isobutylene. (!) indicates resonances assignable to benzonitrile. (&) indicates resonances assignable to **3**. (^) indicates resonances assignable to $\text{HN}=\text{C}(\text{tBu})\text{Ph}$.

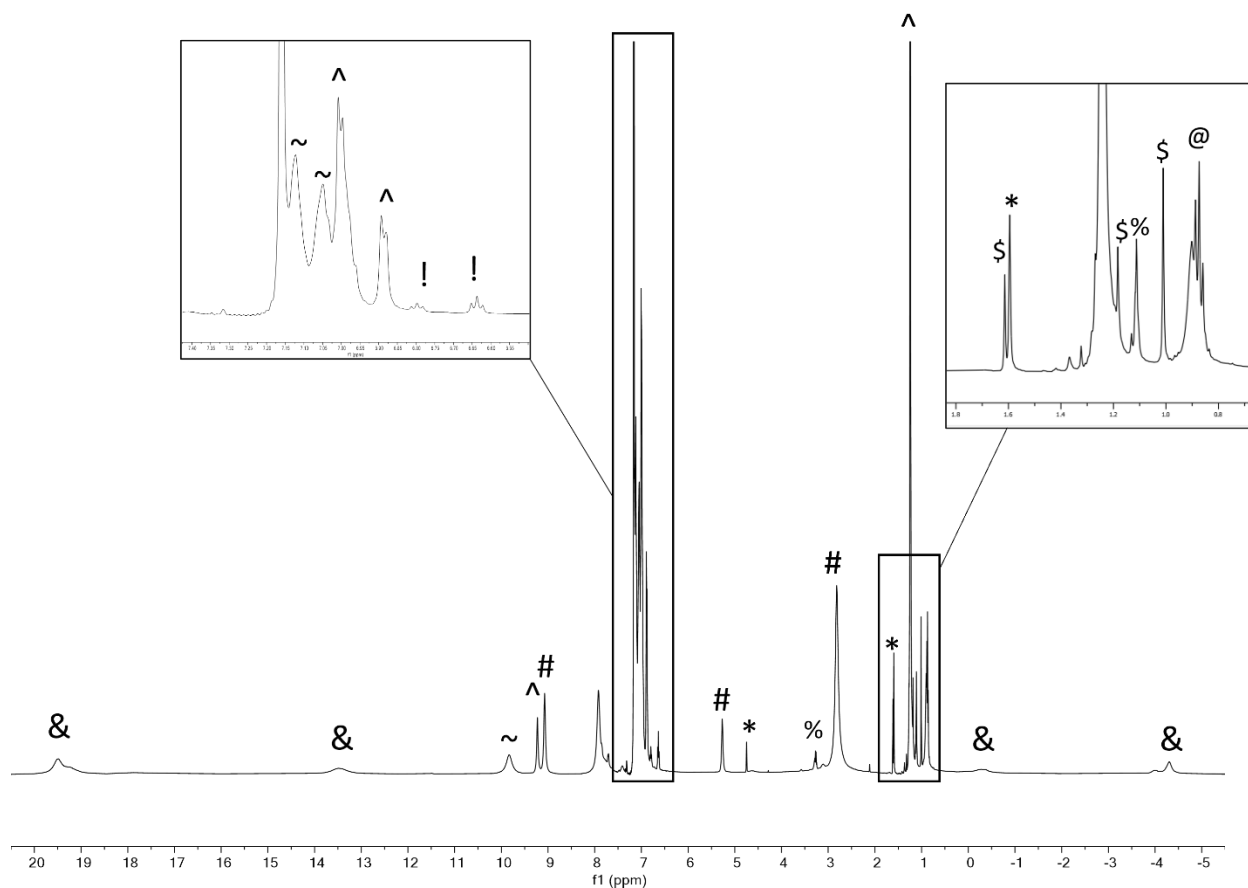


Figure S15. Room temperature ^1H NMR spectrum of the reaction mixture formed by addition of $\text{HN}=\text{CPh}_2$ to **2** in C_6D_6 . (&) indicates resonances assignable to $[\text{Fe}_2(\text{N}=\text{CPh}_2)_6]$.⁴ (*) indicates resonances assignable to vinyl and methyl protons of isobutylene. (!) indicates resonances assignable to benzonitrile. (^) indicates resonances assignable to $\text{HN}=\text{C}(\text{tBu})\text{Ph}$. (#) indicates resonances assignable to unreacted **2**, and (~) indicates resonances assignable to unreacted $\text{HN}=\text{CPh}_2$. (%) indicates resonances assignable to diethyl ether. (@) indicates resonances assignable to hexanes/pentane. (\$) indicates resonances assignable to unidentified products.

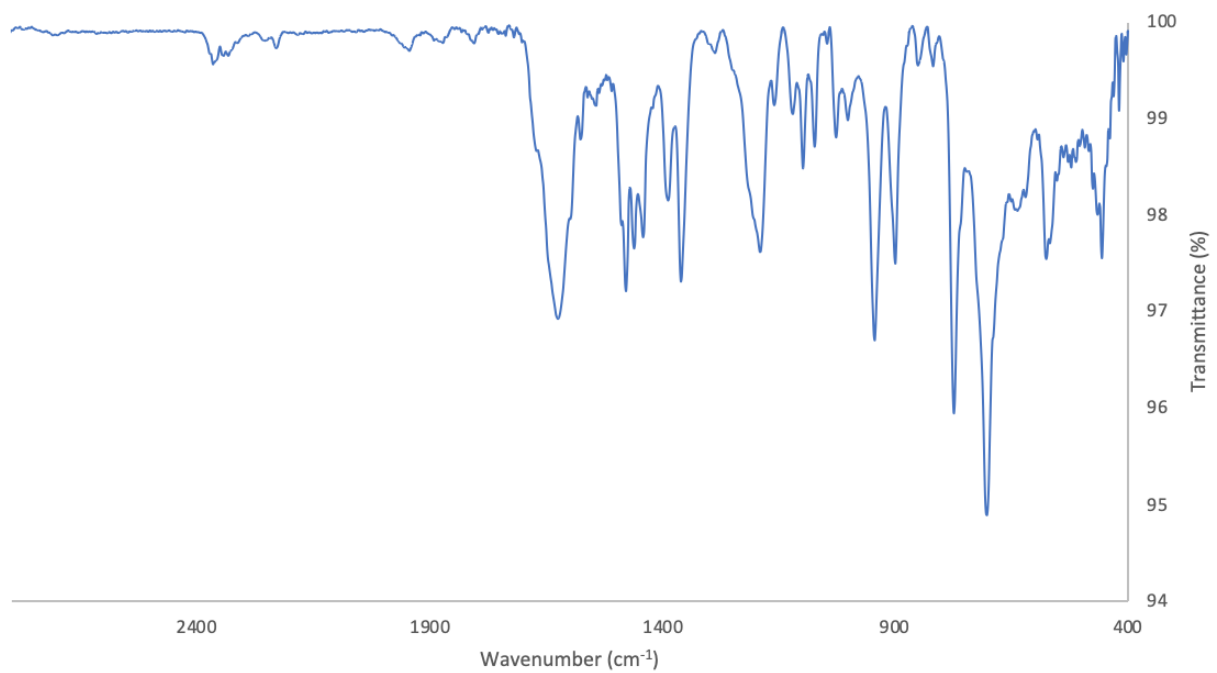


Figure S16. IR spectrum of **1** as a KBr pellet.

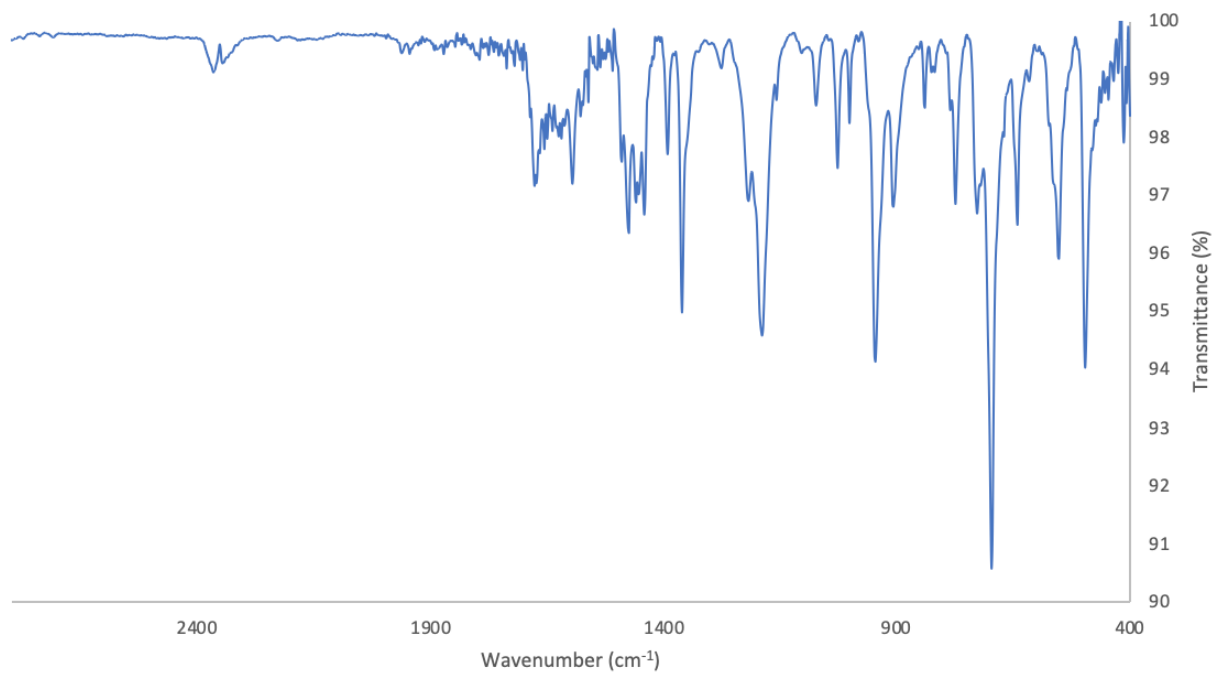


Figure S17. IR spectrum of **2** as a KBr pellet.

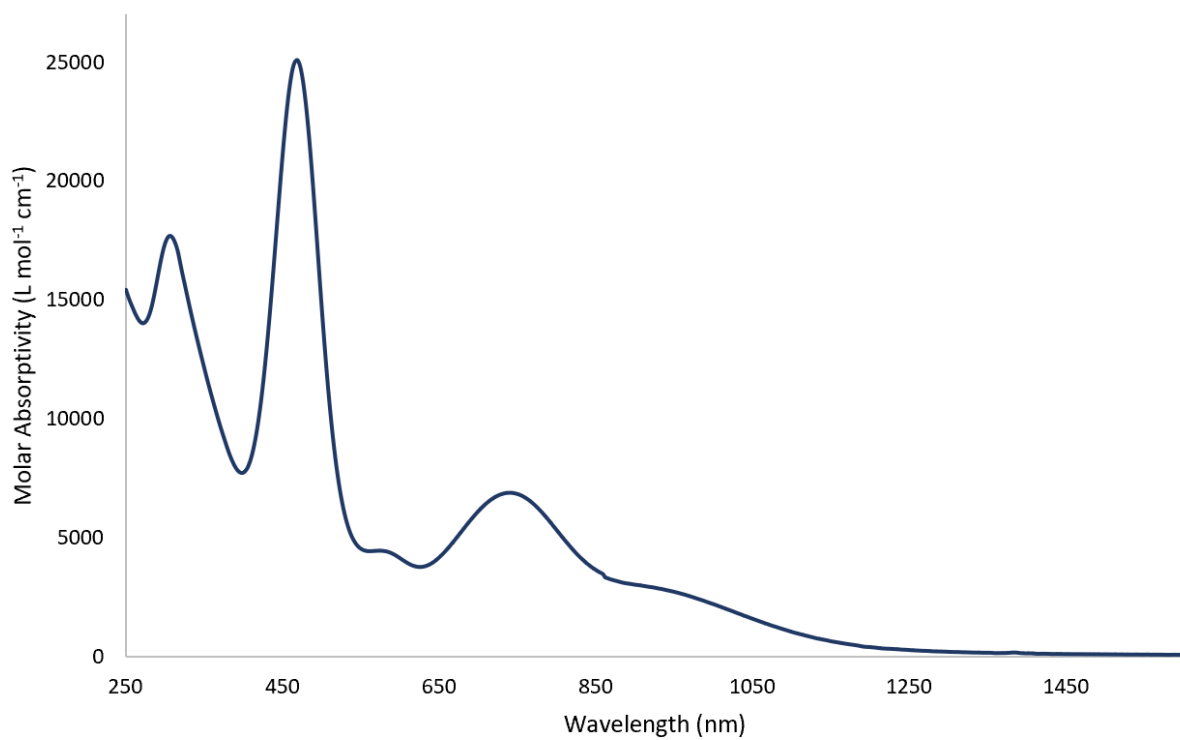


Figure S18. UV-nis/NIR spectrum of **2** (0.1 mM) in pentane.

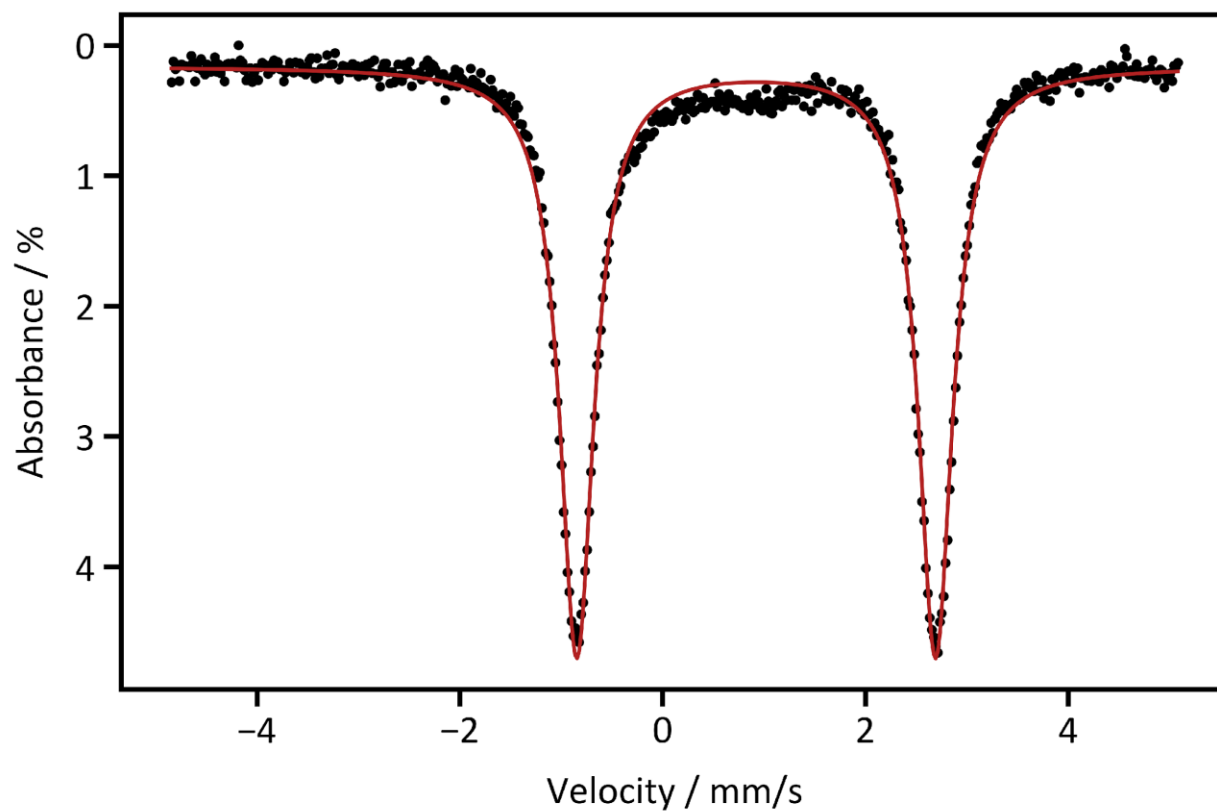


Figure S19. Zero-field ^{57}Fe Mössbauer spectra of **1** collected at $T = 90\text{ K}$. The red trace corresponds to the overall fit of the data, $\delta = 0.924(2)\text{ mm/s}$, $|\Delta E_Q| = 3.537(4)\text{ mm/s}$.

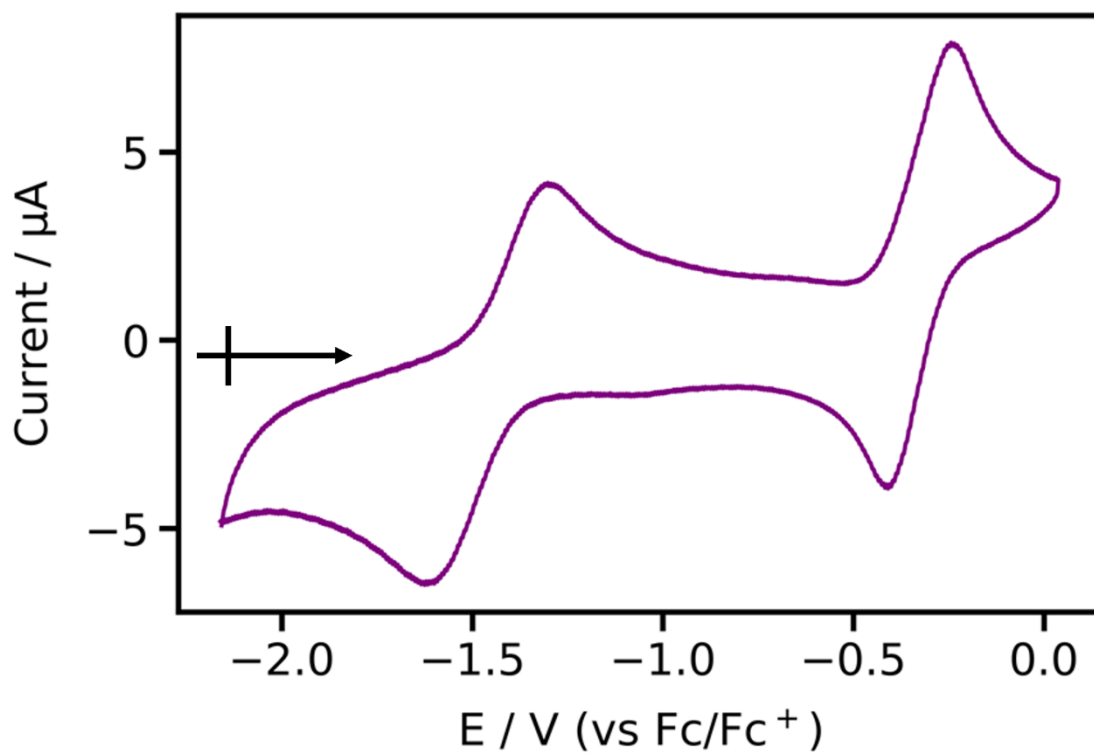


Figure S20. Complete cyclic voltammogram for complex **2** (200 mV/s scan rate). Measured in THF with 0.1 M $[\text{NBu}_4][\text{PF}_6]$ as supporting electrolyte.

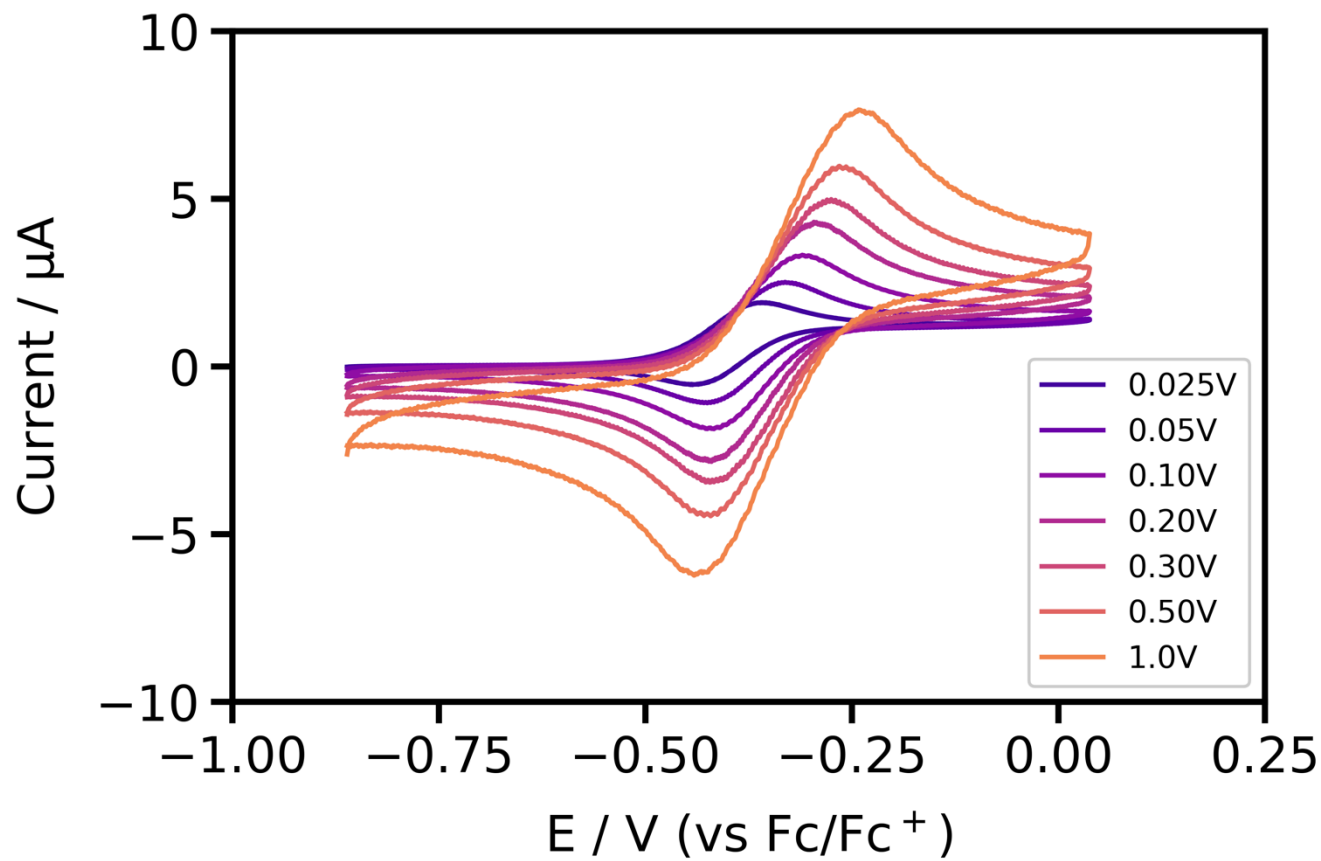


Figure S21. Fe(III)/(IV) couple for complex **2** measured in THF with 0.1 M [NBu₄][PF₆] as supporting electrolyte (vs. Fc/Fc⁺).

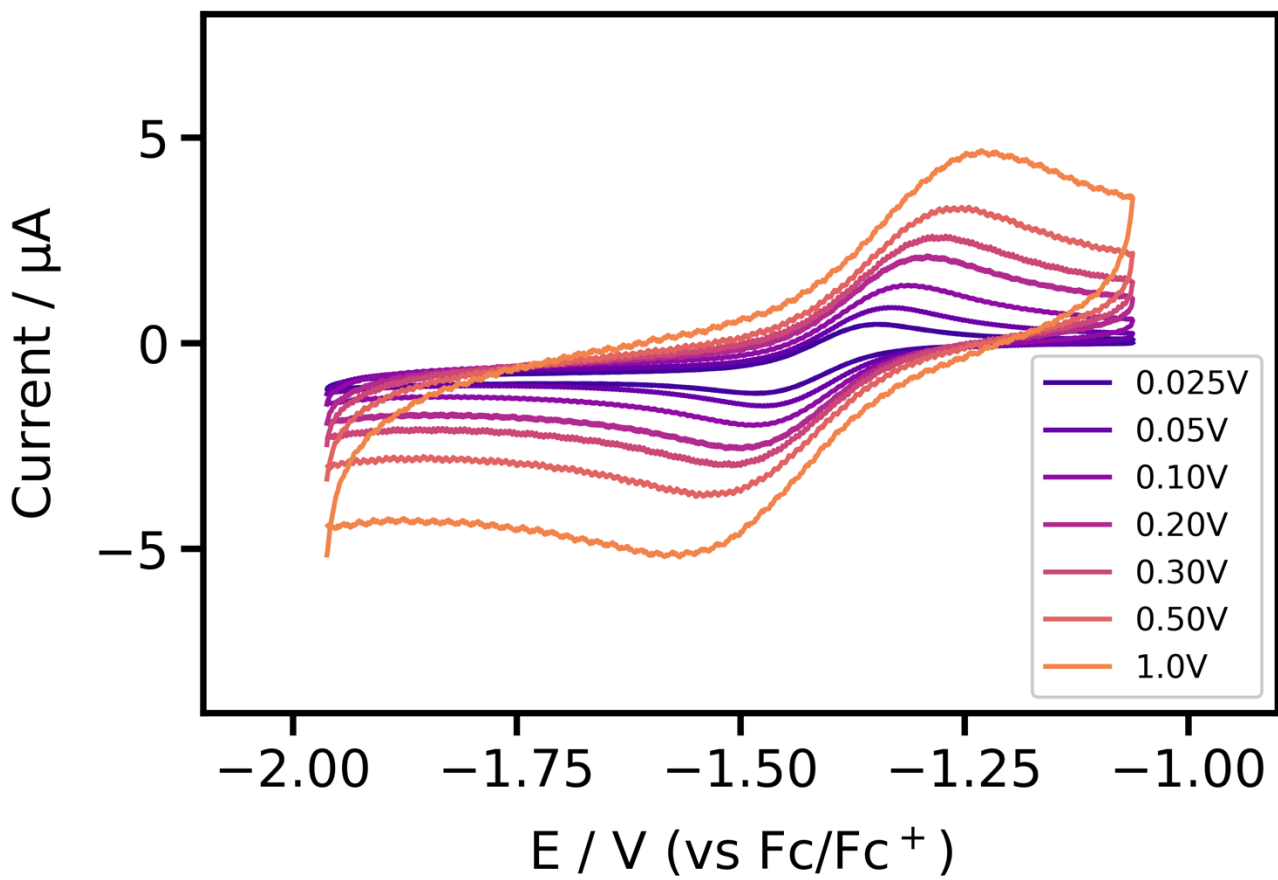


Figure S22. Fe(II)/(III) couple for complex **2** measured in THF with 0.1 M [NBu₄][PF₆] as supporting electrolyte (vs. Fc/Fc⁺).

Table S3. Electrochemical parameters for complex **2** in THF (vs. Fc/Fc⁺, [NBu₄][PF₆] as supporting electrolyte).

Reduction feature 1	Scan rate, V/s	E_{p,c}, V	E_{p,a}, V	ΔE_p^a	i_{p,c}/i_{p,a}
	0.025	-0.360	-0.443	0.083	1.04
	0.05	-0.331	-0.425	0.094	1.06
	0.1	-0.310	-0.417	0.107	1.07
	0.2	-0.296	-0.420	0.124	1.05
	0.3	-0.275	-0.422	0.147	1.04
	0.5	-0.265	-0.421	0.156	1.03
	1.0	-0.242	-0.441	0.199	1.00

Reduction feature 2	Scan rate, V/s	E_{p,c}, V	E_{p,a}, V	ΔE_p^a	i_{p,c}/i_{p,a}
	0.025	-1.344	-1.484	0.140	0.95
	0.05	-1.335	-1.472	0.137	0.99
	0.1	-1.321	-1.487	0.166	1.04
	0.2	-1.292	-1.500	0.208	1.08
	0.3	-1.271	-1.510	0.239	1.11
	0.5	-1.245	-1.550	0.305	1.12
	1.0	-1.231	-1.568	0.337	1.31

^a ΔE_p is defined as the potential difference between the cathodic wave and the anodic wave generated after the change in sweep direction.

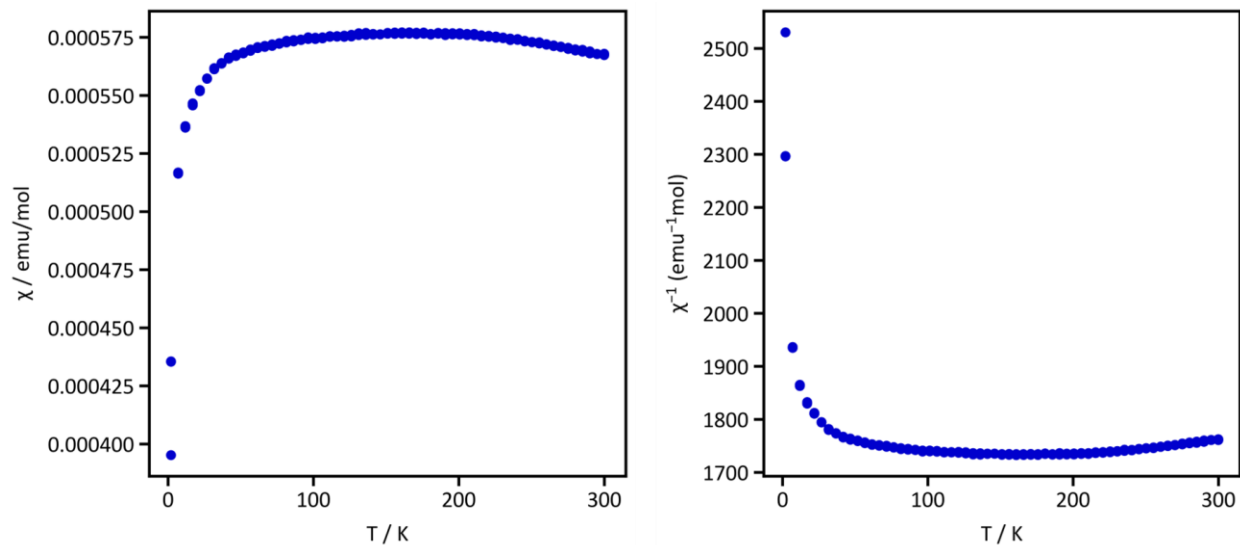


Figure S23. Temperature dependent, solid state magnetic susceptibility (left) and temperature dependent, inverse solid state magnetic susceptibility (right) for **2** collected under an applied field of $H = 1000$ Oe, $m = 35.0$ mg, $M = 696.79$ g/mol.

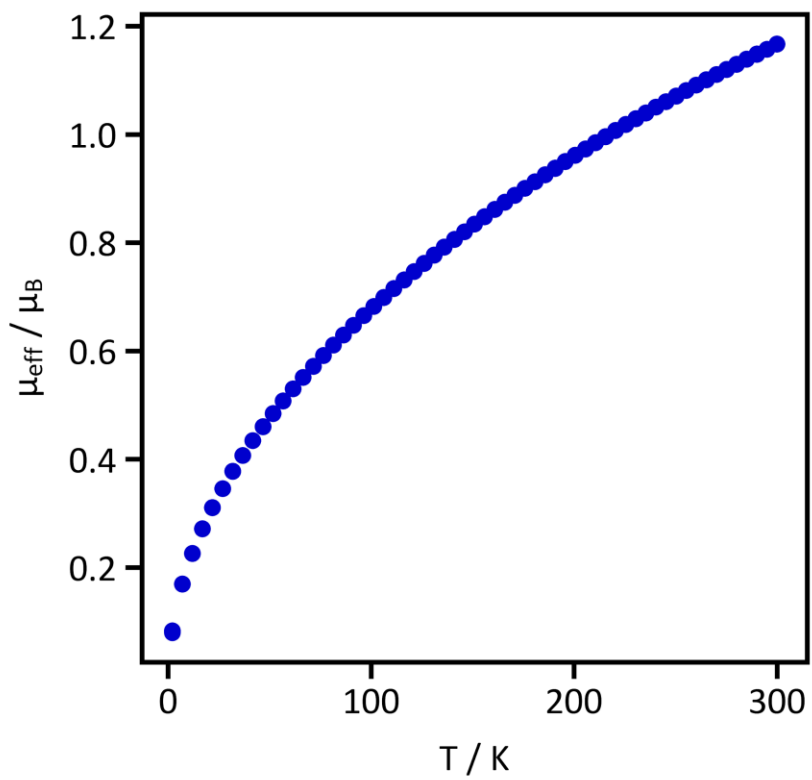


Figure S24. Effective magnetic moment of **2** collected under an applied field of $H = 1000$ Oe.

Computational details

All the geometry optimizations were performed using Kohn-Sham density functional theory (KS-DFT) in Gaussian 16 rev. A03.¹⁵ Geometry optimizations were performed in the gas phase, employing the functionals B3LYP^{16,17}, TPSSh,¹⁸⁻²⁰ and M06-L²¹; including the empirical dispersion correction with Becke and Johnson damping D3BJ to B3LYP and TPSSh.²² The Ahlrich's triple-zeta valence polarized (Def2TZVP) basis set²³ was used for all atoms. The experimental X-ray structure was used as the starting geometry. Vibrational frequency calculations were performed after the optimization step to confirm the absence of imaginary frequencies which relate to local minima. Single point energy calculations were performed using the B3LYP functional including dispersion correction D3BJ with split basis set: Def2QZVP²³ on Fe, Def2TZVPP on N, and Def2TZVP on all the other atoms. All structural optimizations and single point calculations were performed by considering all possible spin state multiplicities of the Fe(IV) center: singlet ($S = 0$), triplet ($S = 1$), and quintet ($S = 2$).

Multireference single-point calculations were performed using the software *OpenMolcas* (v.23.06)²⁴ on both the TPSSh optimized Fe(IV) species (for singlet, triplet, and quintet spin state geometries), and the experimental Fe(IV) crystal structure where the hydrogen atom positions were optimized at the B3LYP-D3BJ/def2-TZVP level of theory. The state-averaged complete active space self-consistent field (SA-CASSCF)²⁵ method was used to compute the singlet, triplet, and quintet state manifolds, obtaining spin-orbit free energies. The active spaces used were (4,5), (4,10), and (9,12). Three post-SA-CASSCF methods, such as state-specific complete active space second order perturbation theory (SS-CASPT2)²⁶ (using an imaginary shift of 0.3 a.u. and ionization-potential electron-affinity shift of 0.25 a.u.); multiconfiguration pair-density functional theory (MC-PDFT)²⁷; and hybrid MC-PDFT²⁸ were employed to compute the relative energies among the various electronic states. Specifically, for MC-PDFT calculations the translated functional tPBE, and the hybrid translated functional tPBE0²⁸ were used. The basis set of choice for all the multiconfiguration single-point calculations was the ANO-RCC-VTZP basis set for the iron center, and ANO-RCC-VDZ basis set²⁹ for the carbon, nitrogen, and hydrogen atoms. The scalar-relativistic effects were included with the second-order Douglas-Kroll-Hess Hamiltonian (DKH2).³⁰ The Cholesky decomposition and the resolution of the identity were used to make the calculations more efficient.³¹

Computational discussion

The experimental magnetic susceptibility data suggest a singlet ground-state and a thermally populated triplet excited state. The B3LYP-D3BJ and M06-L results indicate that the triplet is the ground state, followed by a close lying quintet state; TPSSh-D3BJ instead provides a singlet ground state and a close lying triplet excited state. As described in the main text, the optimization of the complex provides better results than using a geometry from the crystal structure which might contain structural features related to a mix of the singlet and triplet states, thus not ideal to be used for either a net singlet or triplet state (**Table S4**).

Geometry optimizations with different functionals have been performed also to compare the deviations of the optimized structures from the experimental crystal structure. To do so we calculate the root-mean-squared deviation RMSD of the local environment surrounding the Fe center (Fe and four N atoms; **Figure S25**) and of the entire complex (**Figure S26**). All the optimized singlet-state structures display a quasi-planar environment around the iron center. This

is similar to what is observed in the crystal structure. In **Tables S6** and **S7**, we report the computed bond distances, bond angles, and the corresponding experimental data for both singlet and triplet optimized geometries. Starting from the singlet optimized structure; the Fe—N bond distances and N—Fe—N* bond angles computed with M06-L are closer to the experimental data, followed by B3LYP-D3BJ and TPSSh-D3BJ. The bond distances are similarly described by the three functionals. However, the bond angles computed with TPSSh-D3BJ show the largest differences, for example, the computed N—Fe—N* bond angles are 178.6° and 164.6°, and the differences with respect to the experimental structure are 5.6° and 4.9°, respectively, while the differences displayed by B3LYP-D3BJ are 2.3° and 4.1°, and the M06-L differences with the experimental data are 3.2° and 0.8°. When comparing the RMSD between the optimized singlet molecular geometry and the experimental structure (see **Figure S26**), the B3LYP-D3BJ optimized structure has an RMSD of 0.403 Å, while TPSSh-D3BJ and M06-L singlet structures have RMSD values of 1.074 Å and 0.811 Å, respectively. Finally, we observe that the optimized triplet-state molecules have a distorted tetrahedral disposition around the metal center. Also, the optimized quintet structures display a planar environment. All these geometrical features suggest that the overall geometrical description of complex **2** cannot be the same for a net singlet and a net triplet state; therefore, since TPSSh provides a slightly larger deviation between singlet and triplet geometry, and from the experimental crystal structure, this can be the reason for the better energetics and experimental agreement.

When using the crystal structure, the hydrogen atoms are optimized with the functionals used in this work for each spin state considered. In **Table S4**, the singlet is the ground state, followed by the triplet with all functionals. The singlet-triplet gap for B3LYP-D3BJ is 0.424 eV, for TPSSh-D3BJ is 0.560 eV, and for M06-L is 0.425 eV. These singlet-triplet energy gaps are too large for the triplet to be thermally accessible, as a confirmation that a single geometry cannot describe different spin states, even if they are (experimentally) close in energy. In **Table S5** the energy gaps between different optimized geometries are reported, using the different functionals described in the main text, including B3LYP and M06L not discussed there.

Table S5 compares the relative energies between the three spin-states of interest using the B3LYP-D3BJ and TPSSh-D3BJ optimized geometries. The B3LYP-D3BJ relative energies indicate the ground state is a triplet state, followed by the quintet and then the singlet state by 0.08 and 0.19 eV, respectively. However, the experimental magnetic susceptibility measurements do not support the nature of the ground state as a triplet. Using the TPSSh-D3BJ results, the ground state is a singlet state, followed by a triplet and a quintet state, with relative energies of 0.027 and 0.272 eV, respectively. The experimental magnetic susceptibility data suggest a singlet ground state and a low-lying triplet state, similar to the TPSSh-D3BJ results.

The TPSSh-D3BJ geometries are used as input for the multiconfigurational calculations, and the active spaces are displayed in **Figures S27-S29**. Additionally, multireference calculations were performed using TPSSh-D3BJ geometries for each spin state. For the three active spaces considered in this work, the SA-CASSCF method suggests a quintet ground state followed by the triplet and the singlet states (see **Tables S8-S10**). The SS-CASPT2 relative energies indicate the ground state is a singlet and the lowest-lying excited state is a triplet, followed by the quintet state. For these calculations we included, to the already discussed active spaces, the (12,9); although since the 4d orbitals are not included, the results are not satisfactory but reported for completeness.

The singlet-triplet gap for the active spaces (4,5), (4,10), and (12,9) are 0.109, 0.106 (**Table 1** main text), and 0.752 eV, respectively. The trend of the tPBE results is consistent with the SS-CASPT2 data; the tPBE singlet-triplet energy gaps are 0.366, 0.387, and 1.038 eV respectively at the previously listed active spaces. Regarding the tPBE0 results, for (4,5) and (4,10) active spaces, the ground state is the triplet and the first excited state is the singlet, the computed energy gaps between these states are 0.058 and 0.017 eV (**Table 1**, main text). This implies that the triplet and singlet states are closely degenerate. Again, for the (12,9) active space, tPBE0 agrees with tPBE and SS-CASPT2, indicating the singlet is the ground state and the triplet the first excited state with an energy gap of 0.694 eV.

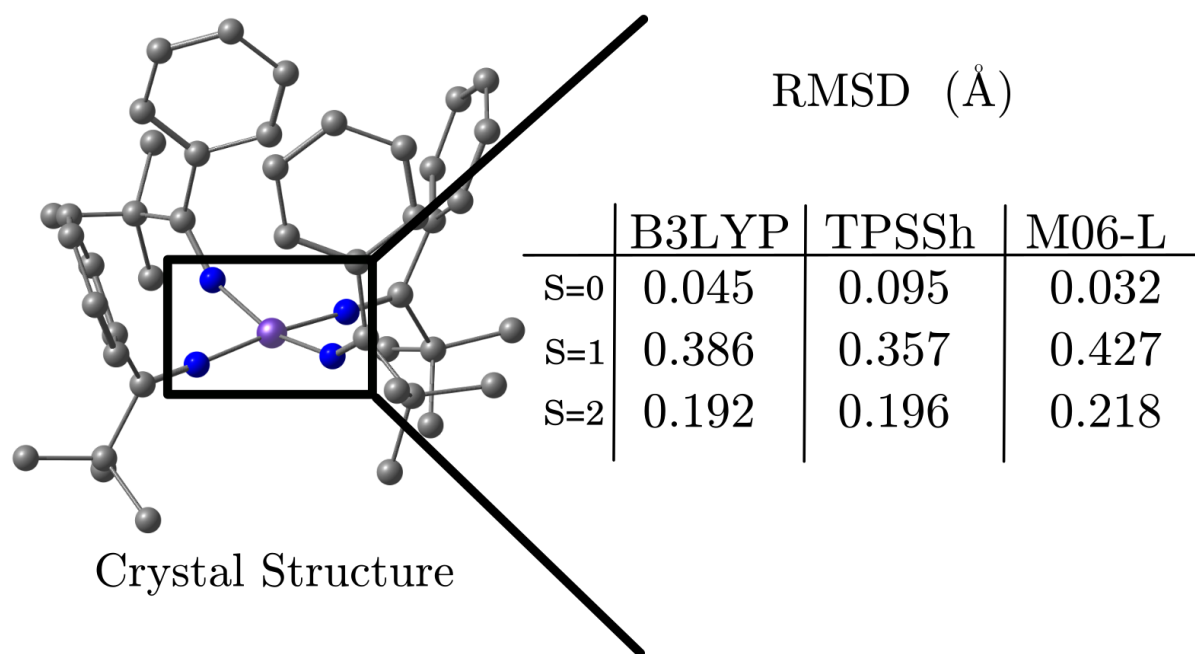


Figure S25. Comparison between the Fe(IV) environment considering only Fe and four N atoms of the structure from the experimental crystal structure with the DFT optimized structures with the B3LYP-D3BJ, TPSSh-D3BJ, and M06-L functionals at the singlet, triplet, and quintet spin states. The RMSD values were computed only for the Fe and N atoms. Hydrogen atoms are omitted for clarity. Color code = Fe: purple, C: grey, N: blue.

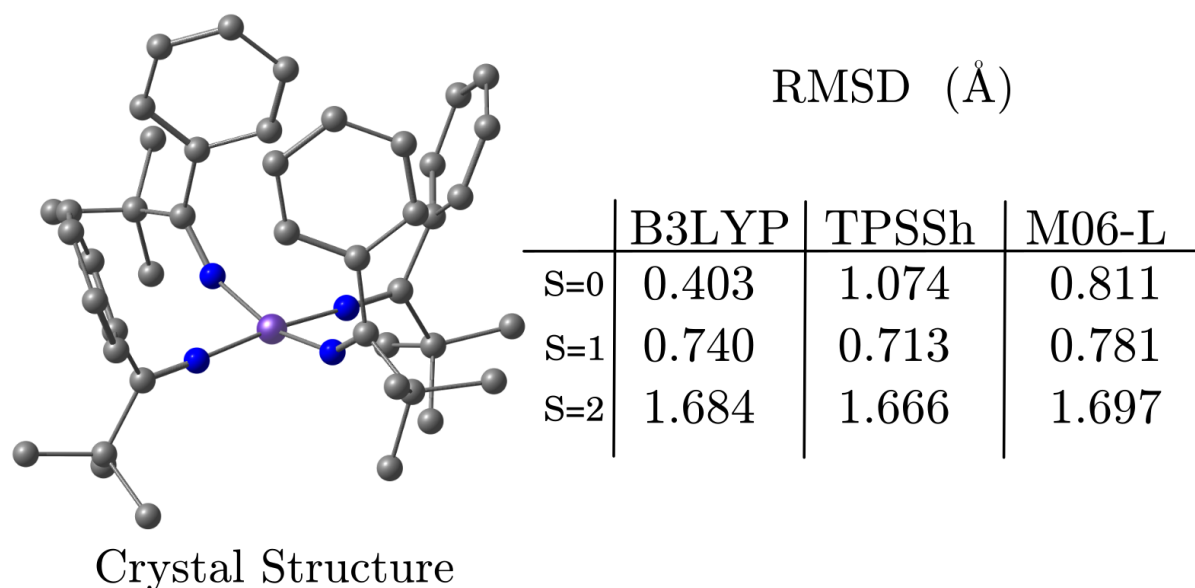


Figure S26. Comparison between a single molecule obtained from the crystal structure and the DFT optimized structures with the B3LYP-D3BJ, TPSSh-D3BJ, and M06-L functionals at the singlet, triplet, and quintet spin states. The RMSD values were computed considering all atomic positions. Hydrogen atoms are omitted for clarity. Color code = Fe: purple, C: grey, N: blue.

Table S4. Relative electronic energies in eV between the lowest singlet, triplet, and quintet states. For each functional, using the crystal structure. The triplet and quintet states energies are obtained after optimizing only the hydrogen atoms positions for each spin state.

Spin State	B3LYP-D3BJ (eV)	TPSSh-D3BJ (eV)	M06-L (eV)
Singlet	0.000	0.000	0.000
Triplet	0.424	0.560	0.425
Quintet	0.553	0.831	0.722

Table S5. Relative electronic energies in eV between the optimized singlet, triplet, and quintet states geometries with the listed functionals, and def2-TZVP basis set. The TPSSh column is the same as in **Table 1** of the main text.

Spin State	B3LYP-D3BJ (eV)	TPSSh-D3BJ (eV)	M06-L (eV)
Singlet	0.190	0.000	0.152
Triplet	0.000	0.027	0.000
Quintet	0.082	0.272	0.042

Table S6. Experimental bond distances and bond angles between the iron and the nitrogen atoms. The computational values correspond to the DFT optimized singlet state structures with the B3LYP-D3BJ, TPSSh-D3BJ, and M06-L functionals and def2-TZVP basis set.

Bond distances				
Parameter	X-ray (Å)	B3LYP-D3BJ (Å)	TPSSh-D3BJ (Å)	M06-L (Å)
N1-Fe	1.757	1.749	1.752	1.758
N1*-Fe	1.757	1.749	1.752	1.758
N2-Fe	1.786	1.776	1.758	1.782
N2*-Fe	1.786	1.776	1.758	1.782
Bond angles				
N1-Fe-N1*	172.96	170.68	178.55	169.81
N2-Fe-N2*	159.70	155.65	164.60	158.90

Table S7. Experimental bond distances and bond angles between the iron and the nitrogen atoms. The computational values correspond to the DFT optimized triplet state structures with the B3LYP-D3BJ, TPSSh-D3BJ, and M06-L functionals and def2-TZVP basis set.

Bond distances				
Parameter	X-ray (Å)	B3LYP-D3BJ (Å)	TPSSh-D3BJ (Å)	M06-L (Å)
N1-Fe	1.757	1.759	1.740	1.768
N1*-Fe	1.757	1.759	1.741	1.768s
N2-Fe	1.786	1.811	1.799	1.832
N2*-Fe	1.786	1.811	1.799	1.832
Angles				
N1-Fe-N1*	173.0	135.12	135.46	135.62
N2-Fe-N2*	159.7	141.954	145.6	136.04

Multiconfigurational Calculations

The electronic configuration of the metal center, Fe(IV), is $3d^4$. The minimal active space consists of 4 electrons in the five $3d$ orbitals (4,5) (**Figure S27**). By adding a correlating subshell of d orbitals, we obtain (4,10) active space (**Figure S28**). Also, we can add iron—ligand occupied orbitals to the minimal active space, yielding the (12,9) active space (**Figure S29**).

When computing the state-averaged energies, we considered 5 quintets, 35 triplets, and 22 singlets. Each state has the same weight in the SA-CASSCF calculations. After the state-averaged calculations, we include relativistic effects through spin-orbit coupling (SOC) for the computation of magnetic properties. We used the restricted active space state interaction (RASSI) approach^{32–34} to include SOC perturbatively after the SA-CASSCF (SA-CASSCF-SO), SS-CASPT2 (SS-CASPT2-SO), MC-PDFT (tPBE-SO) and hybrid MC-PDFT (tPBE0-SO) calculations, by using the protocol discussed in Ref.³⁵. We then used the *SINGLE_ANISO*³⁶ module to compute the magnetic susceptibility (χT), for the spin-orbit states obtained with the methods mentioned before.

Table S8. Single point calculations using the TPSSh optimized structures of the singlet, triplet, and quintet spin states, at CASPT2 and MC-PDFT multireference levels with the (4,5) active space. The relative energies are in eV.

Spin state	TPSSh (opt)	SA-CASSCF	SS-CASPT2	tPBE	tPBE0
Singlet	0.000	2.841	0.000	0.000	0.058
Triplet	0.027	1.513	0.109	0.366	0.000
Quintet	0.272	0.000	2.255	1.821	0.713

Table S9. Single point calculations using the TPSSh optimized structures of the singlet, triplet, and quintet spin states, at CASPT2 and MC-PDFT multireference levels with the (4,10) active space. The relative energies are in eV.

Spin state	TPSSh (opt)	SA-CASSCF	SS-CASPT2	tPBE	tPBE0
Singlet	0.000	3.211	0.000	0.000	0.017
Triplet	0.027	1.979	0.106	0.387	0.000
Quintet	0.272	0.000	3.924	3.497	1.838

Table S10. Single point calculations using the TPSSh optimized structures of the singlet, triplet, and quintet spin states, at CASPT2 and MC-PDFT multireference levels with the (12,9) active space. The relative energies are in eV.

Spin state	TPSSh (opt)	SA-CASSCF	SS-CASPT2	tPBE	tPBE0
Singlet	0.000	0.759	0.000	0.000	0.000
Triplet	0.027	0.422	0.752	1.038	0.694
Quintet	0.272	0.000	1.375	2.701	1.838

Tables S8-S10 report the singlet-triplet energy gaps computed with SA-CASSCF, SS-CASPT2, tPBE, and tPBE0 using the active spaces shown in **Figures S27-S29** and the TPSSh-D3BJ optimized geometries. The CASPT2 and tPBE methods consistently suggest the ground state is a singlet and the first excited state is a triplet state with energy gaps greater than zero. The SS-CASPT2 singlet-triplet gaps are 0.109, 0.106, and 0.752 eV for (4,5), (4,10), and (12,9) active spaces, respectively. Similarly, the tPBE0 energy gaps are -0.058, -0.017 and 0.694 eV, for the active spaces aforementioned. No systematic improvement in the energy gaps is observed with increasing the active space.

The occupation numbers for the singlet state shown in **Figures S27-S29** indicate the ground state is a closed-shell singlet state because the occupied orbitals display occupation numbers close to 2.

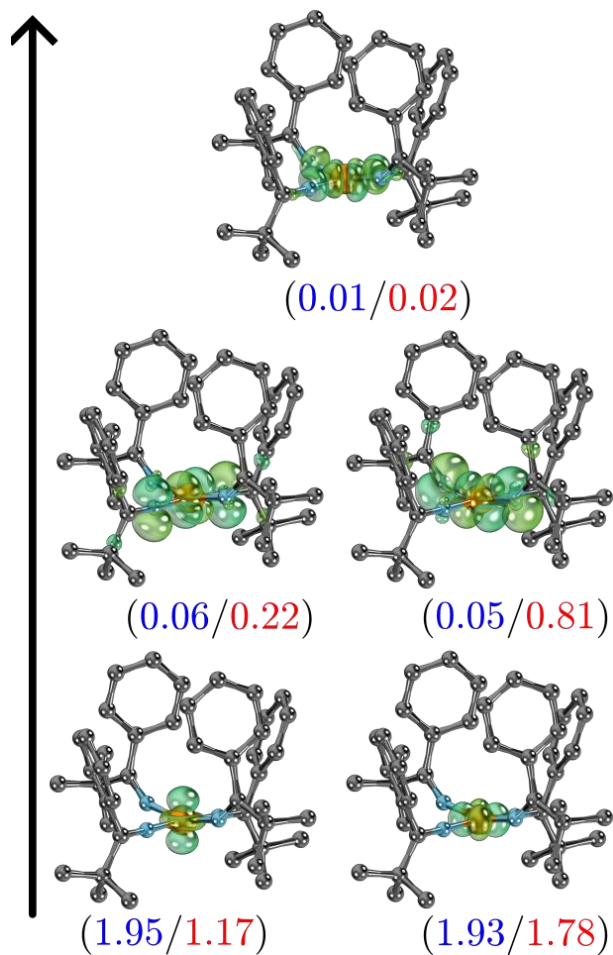


Figure S27. Molecular orbitals in the (4,5) active space of complex **2**. In blue, the occupation numbers for the singlet ground state, and in red, the occupation numbers for the first triplet excited state. Hydrogen atoms are omitted for clarity.

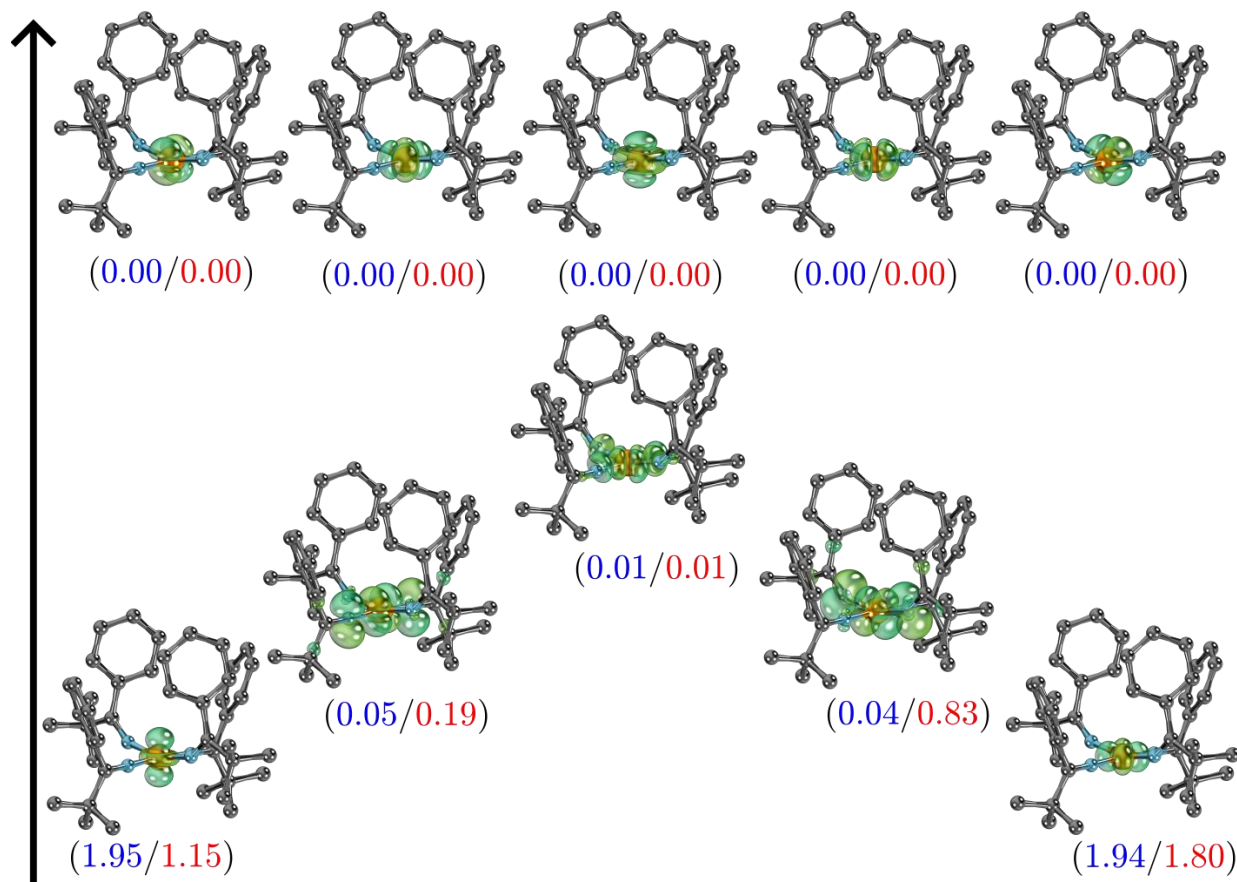


Figure S28. Molecular orbitals in the (4,10) active space of complex 2. In blue, the occupation numbers for the singlet ground state, and in red, the occupation numbers for the first triplet excited state. Hydrogen atoms are omitted for clarity.

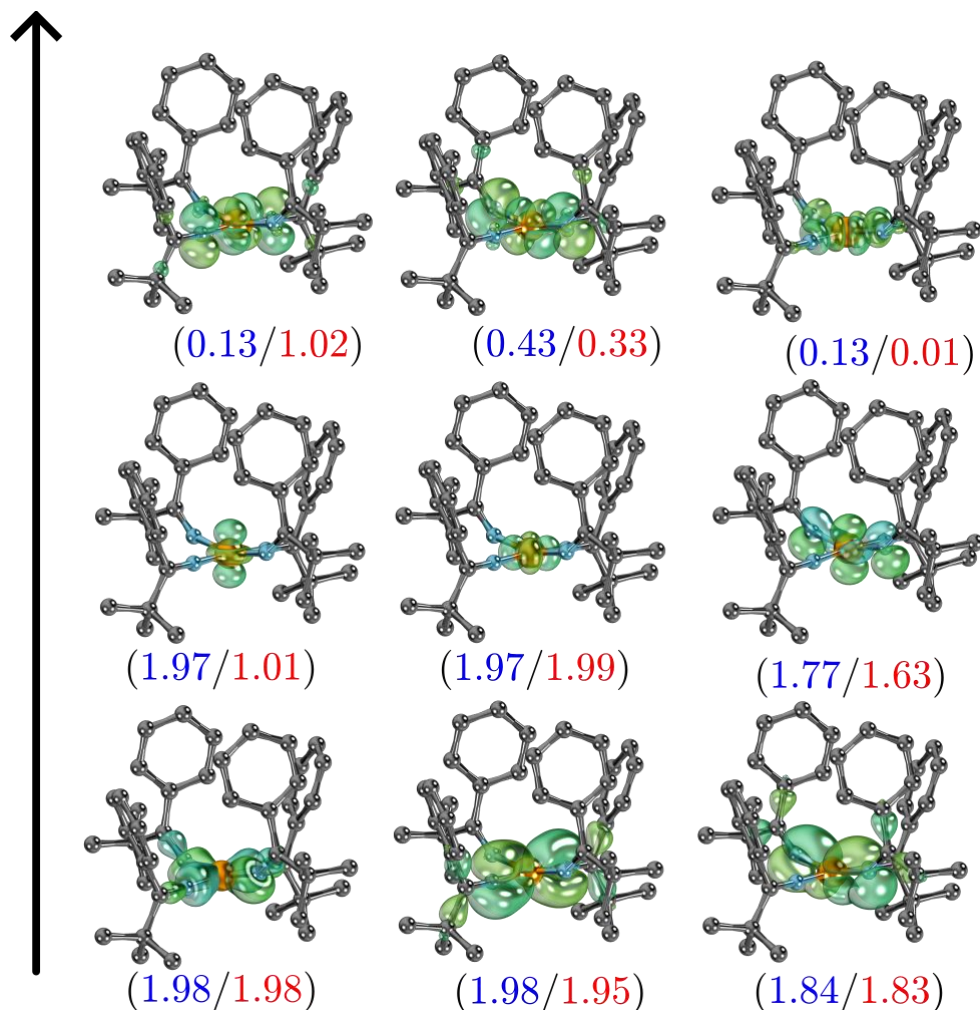


Figure S29. Molecular orbitals in the (12,9) active space of complex **2**. In blue, the occupation numbers for the singlet ground state, and in red, the occupation numbers for the first triplet excited state. Hydrogen atoms are omitted for clarity.

The computed magnetic susceptibility with SA-CASSCF-SO, SS-CASPT2-SO, and tPBE-SO methods are shown in **Figure S30**. Notably, in panel **A**, when using the (4,5) active space, SA-CASSCF-SO (red) is predicting a quintet ground state, which is not in agreement with experiments of the complex **2** ground state. In **Figure S30**, panel **B**, we observe the SA-CASSCF-SO plot is the same as the corresponding red line in panel **A**. However, in **Figure S30** panel **C**, the SA-CASSCF-SO curve displays a behavior in between a triplet and a quintet state. This is due to the small energy differences between the triplet and quintet state (~ 0.01 eV) when using the (12,9) active space reported in **Table S13**. There is a small improvement when increasing the active space size for the SA-CASSCF-SO results, because for (4,5) and (4,10) active spaces, the ground state is a quintet state, but when including metal-ligand molecular orbitals to get (12,9) active space, we obtain a triplet state (**Tables S11-S13**). Still, the SA-CASSCF-SO results are incorrect because they do not support the experimental χ_T curve. SS-CASPT2-SO and tPBE0-SO correctly describe the linear behavior of χ_T for all active spaces. Therefore, for complex **2** it is important to include dynamic correlation.

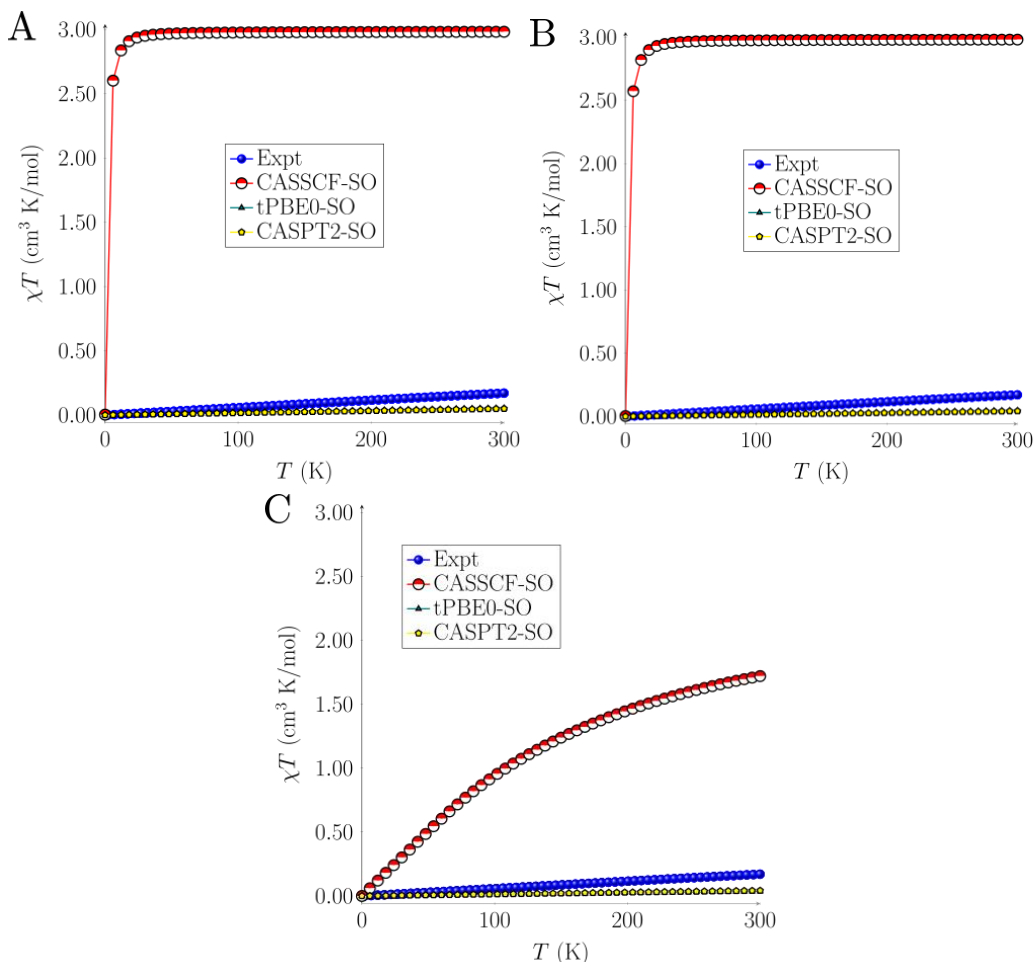


Figure S30. Magnetic susceptibility of complex **2**. Experimental data (blue) is obtained with a magnetic field of 0.1 T. The magnetic susceptibility (χT) was computed with SA-CASSCF-SO (red), SS-CASPT2-SO (yellow), and tPBE0-SO (green) employing the singlet optimized structure with TPSSh-D3BJ/def2-TZVP. **A:** Results using (4,5) active space. **B:** Results using (4,10) active space. **C:** Results using (12,9) active space.

Comparing the post-SA-CASSCF-SO results with the experimental data in **Figure S31** panels **A**, **B**, and **C**, the main observation is that the computed χT values with all methods are linear functions of the temperature. The tPBE0-SO and SS-CASPT2-SO linear functions have similar slopes, and tPBE-SO has a slightly lower slope than the tPBE0-SO and SS-CASPT2-SO methods. The experimental data has a larger slope than all the computational methods. We can observe in **Figure S31** that increasing the active space has no improvement in the computed χT linear functions. The experimental data has a slope of $\chi \sim 0.00057 \text{ cm}^3/\text{mol}$, while the computational methods present an approximate slope of $\chi \sim 0.00015 \text{ cm}^3/\text{mol}$.

The magnetic susceptibility curves were computed using also additional structures. **Figure S32** displays the χT plots for the three active spaces considered in this work using the B3LYP-D3BJ singlet optimized structure. The three plots shown in panels **A**, **B**, and **C** are similar to the figures shown in **Figure S30**.

Figures S35-S36 present the χT curves obtained using the optimized triplet structures with TPSSh-D3BJ, and B3LYP-D3BJ, respectively. Note that the computed curves are not linear like the experimental data. For all methods and active spaces, the χT curves have an asymptotic behavior.

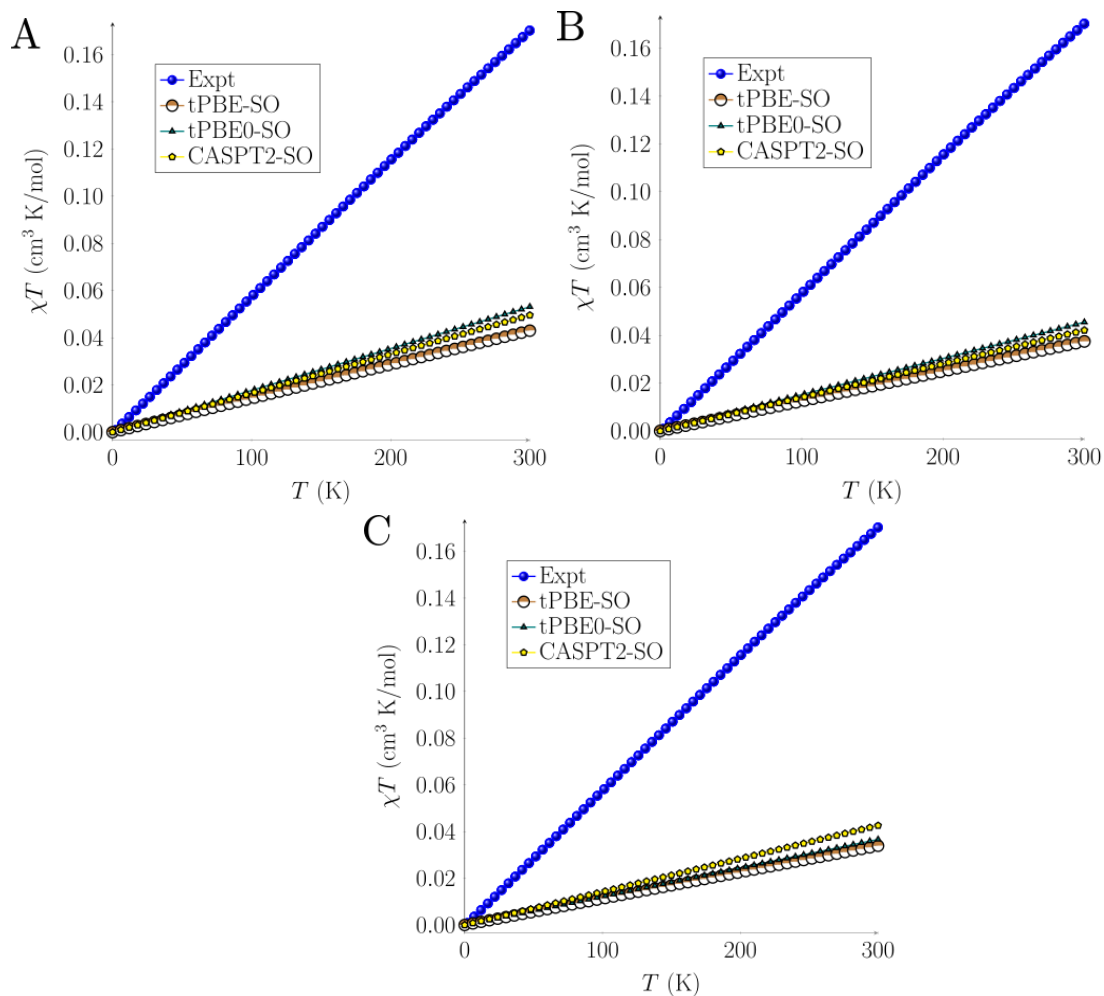


Figure S31. Magnetic susceptibility of complex **2**. Experimental data (blue) is obtained with a magnetic field of 0.1 T. The magnetic susceptibility was computed with SS-CASPT2-SO (yellow), tPBE-SO (brown), and tPBE0-SO (green) using the singlet optimized structure with TPSSh-D3BJ/def2-TZVP. **A:** Results using (4,5) active space. **B:** Results using (4,10) active space. **C:** Results using (12,9) active space.

Table S11. Calculated relative energies between the singlet, triplet, and quintet lowest-lying states. The relative energies (in eV) were computed with SA-CASSCF, SS-CASPT2, and tPBE0 for the singlet state optimized geometry with TPSSh-D3BJ. The values were obtained using the (4,5) active space.

	SA-CASSCF [eV]	SS-CASPT2 [eV]	tPBE [eV]	tPBE0 [eV]
Singlet	2.276	0.000	0.000	0.000
Triplet	1.865	0.683	1.022	0.664
Quintet	0.000	1.916	2.002	0.932

Table S12. Calculated relative energies between the singlet, triplet, and quintet lowest-lying states. The relative energies (in eV) were computed with SA-CASSCF, SS-CASPT2, and tPBE0 for the singlet state optimized geometry with TPSSh-D3BJ. The values were obtained using the (4,10) active space.

	SA-CASSCF [eV]	SS-CASPT2 [eV]	tPBE [eV]	tPBE0 [eV]
Singlet	1.866	0.000	0.000	0.000
Triplet	1.601	0.808	1.072	0.738
Quintet	0.000	2.359	2.383	1.091

Table S13. Calculated relative energies between the singlet, triplet, and quintet lowest-lying states. The relative energies (in eV) were computed with SA-CASSCF, SS-CASPT2, and tPBE0 for the singlet state optimized geometry with TPSSh-D3BJ. The values were obtained using the (12,9) active space.

	SA-CASSCF [eV]	SS-CASPT2 [eV]	tPBE [eV]	tPBE0 [eV]
Singlet	0.053	0.000	0.000	0.000
Triplet	0.000	0.648	0.944	0.695
Quintet	0.005	2.738	3.662	2.734

Table S14. The lowest-lying 20 spin-orbit state energies were computed with SA-CASSCF-SO, SS-CASPT2-SO, tPBE-SO, and tPBE0-SO when using the (4,5) active space. The energies are in cm^{-1} .

SO state	SA-CASSCF-SO	SS-CASPT2-SO	tPBE-SO	tPBE0-SO
1	0.0000	0.0000	0.0000	0.0000
2	0.0890	4675.6421	8187.0296	5290.2479
3	10.9903	4695.0565	8217.8466	5346.4575
4	12.0765	4721.3090	8280.4343	5391.3036
5	15.3802	5581.1473	8296.8862	5437.4216
6	14864.7679	5586.6579	8359.9644	5502.2518
7	15021.9860	5608.4371	8362.4422	5527.3466
8	15045.7111	7315.5948	9904.3344	7584.4912
9	15214.3279	7325.5799	9914.7752	7584.7512
10	15233.1545	7332.2631	9919.2940	7591.0166
11	15235.7306	7971.2943	10481.5618	7614.1152
12	17762.4047	7998.5531	10515.3827	7616.0022
13	17767.4048	8005.7544	10519.2464	7859.7320
14	17792.5212	13244.6018	15609.7997	7867.8302
15	18360.7906	14060.4359	15756.9446	7877.9644

16	18365.9381	15550.4065	16204.4203	8360.3654
17	18375.6895	15554.8466	16209.2939	8414.8155
18	18502.8561	15555.0234	16210.1010	8417.6011
19	19673.9182	15568.5435	16225.4401	12481.0558
20	19706.8045	15568.5670	16225.4817	12616.7179

Table S15. The lowest-lying 20 spin-orbit state energies were computed with SA-CASSCF-SO, SS-CASPT2-SO, tPBE-SO, and tPBE0-SO when using the (4,10) active space. The energies are in cm^{-1} .

SO state	SA-CASSCF-SO	SS-CASPT2-SO	tPBE-SO	tPBE0-SO
1	0.0000	0.0000	0.0000	0.0000
2	0.1006	5924.2891	8631.8256	5947.8625
3	11.8245	5946.5348	8655.5544	5987.3327
4	12.8145	5959.5639	8680.7639	5996.7806
5	16.4199	6577.6403	8863.5430	6192.2974
6	12711.5215	6580.5025	8882.5555	6221.8699
7	12902.5414	6597.7381	8886.2150	6224.3903
8	12921.5771	8124.1593	10081.6824	8147.1422
9	13164.7181	8138.3717	10095.9154	8155.3819
10	13174.1433	8144.7289	10099.1825	8159.2145
11	13187.7281	9253.2135	10943.8312	8877.5241
12	15255.5236	9273.1946	10971.3319	8897.3710
13	16528.6763	9280.5718	10974.4448	8902.3560
14	16543.7370	14984.2493	17017.0711	10331.7151
15	16545.1064	15391.7414	17303.6075	10340.9669

16	17021.7852	18744.6507	18488.4878	10345.6223
17	17082.7737	18748.2057	18722.3263	10377.7205
18	17161.6709	18748.3823	18725.9766	10378.0637
19	17282.4249	18759.2833	18726.6261	13821.2466
20	17385.6921	18759.2921	18738.1369	14066.5238

Table S16. The lowest-lying 20 spin-orbit state energies were computed with SA-CASSCF-SO, SS-CASPT2-SO, tPBE-SO, and tPBE0-SO when using the (12,9) active space. The energies are in cm^{-1} .

SO state	SA-CASSCF-SO	SS-CASPT2-SO	tPBE-SO	tPBE0-SO
1	0.0000	0.0000	0.0000	0.0000
2	148.5606	5273.1186	7645.7405	5646.0284
3	171.8924	5275.4343	7646.9723	5647.1278
4	401.6041	5299.4168	7660.3499	5669.5057
5	401.9256	6398.7479	9462.0543	9279.7063
6	475.1038	6404.7126	9467.3094	9282.5246
7	588.3198	6412.5914	9469.3910	9292.2580
8	618.2339	8825.2804	10425.9951	9446.4856
9	1038.6811	8830.4477	10436.7406	9459.9570
10	3326.1289	8832.7269	10437.1776	9467.2906
11	3342.4275	9668.5864	11515.5630	10630.9305
12	3369.0657	9701.9455	11517.1496	10649.5824
13	3832.7134	9704.0396	11522.4436	10651.8573
14	3833.4365	10284.9240	11676.8064	11810.9116
15	3842.2877	11060.3050	11717.0861	11829.0148

16	3847.9296	11061.1734	11722.7056	11833.6713
17	3849.8144	11066.2323	13985.2273	13732.2352
18	5041.0817	13396.0885	15914.2383	14316.6203
19	5043.8627	15209.1856	16268.5842	14842.8263
20	5060.0720	15237.0041	16642.4384	14860.3666

Additional magnetic susceptibility plots
-Optimized singlet structure

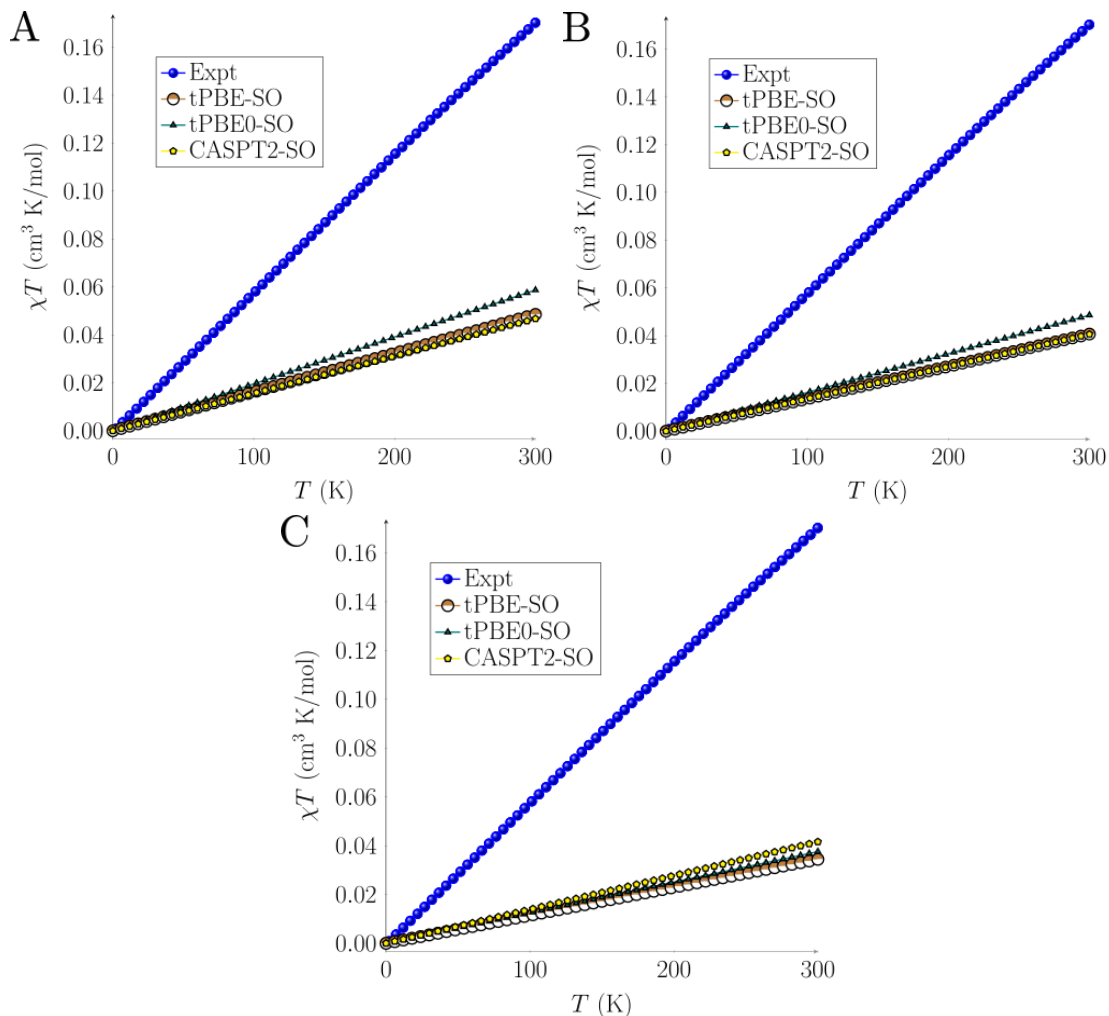


Figure S32. Magnetic susceptibility of complex **2**. Experimental data (blue) is obtained with a magnetic field of 0.1 T. The magnetic susceptibility was computed with SS-CASPT2-SO (yellow), tPBE-SO (brown), and tPBE0-SO (green) using the singlet optimized structure with B3LYP-D3BJ/def2-TZVP. **A:** Results using (4,5) active space. **B:** Results using (4,10) active space. **C:** Results using (12,9) active space.

-Optimized triplet structure

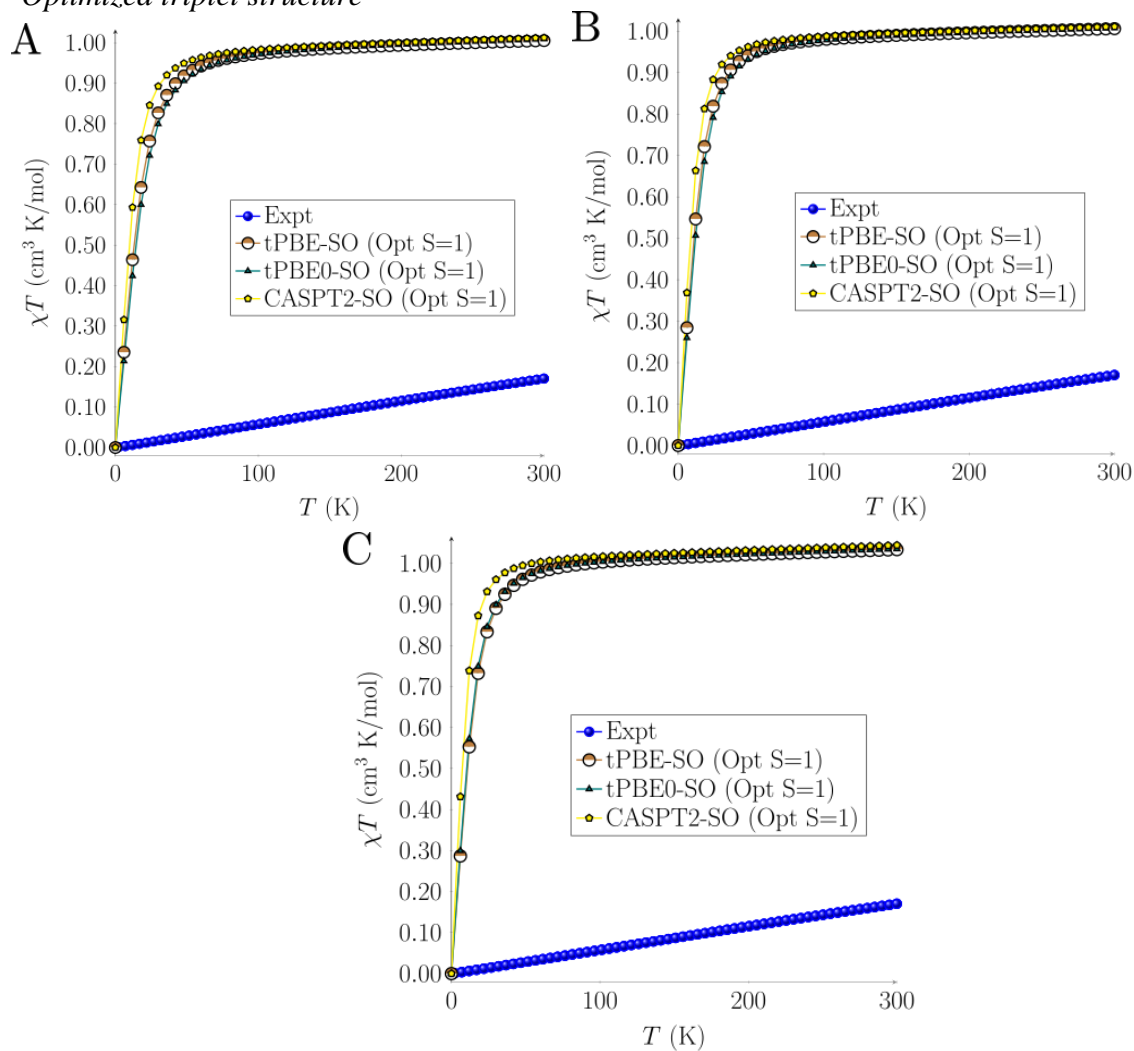


Figure S33. Magnetic susceptibility of complex **2**. Experimental data (blue) is obtained with a magnetic field of 0.1 T. The magnetic susceptibility was computed with SS-CASPT2-SO (yellow), tPBE-SO (brown), and tPBE0-SO (green) using the triplet optimized structure with TPSSh-D3BJ/def2-TZVP. **A:** Results using (4,5) active space. **B:** Results using (4,10) active space. **C:** Results using (12,9) active space.

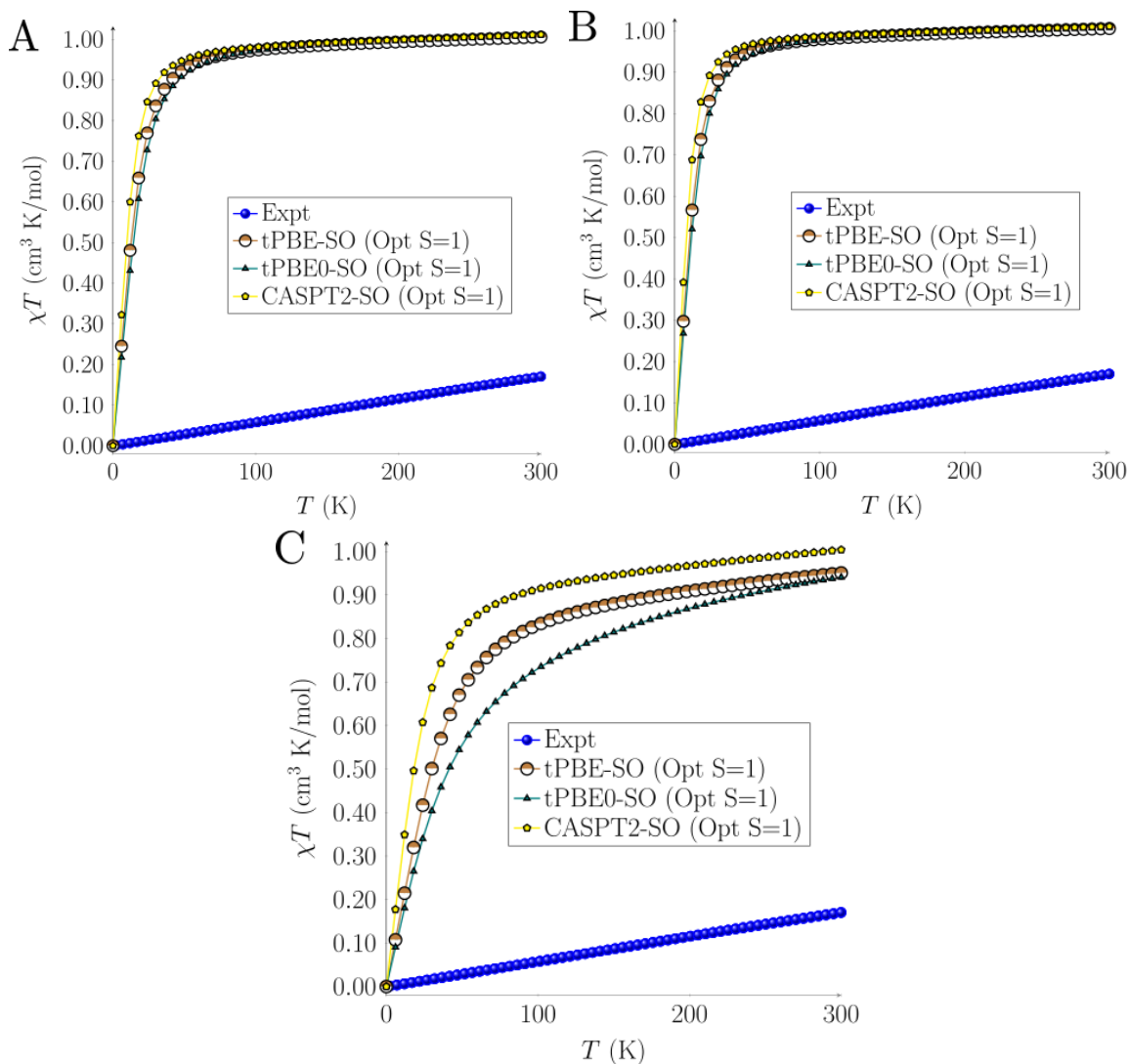


Figure S34. Magnetic susceptibility of complex **2**. Experimental data (blue) is obtained with a magnetic field of 0.1 T. The magnetic susceptibility was computed with SS-CASPT2-SO (yellow), tPBE-SO (brown), and tPBE0-SO (green) using the triplet optimized structure with B3LYP-D3BJ/def2-TZVP. **A:** Results using (4,5) active space. **B:** Results using (4,10) active space. **C:** Results using (12,9) active space.

References

- (1) Barr, D.; Clegg, W.; Mulvey, R. E.; Snaith, R.; Wade, K. Bonding Implications of Interatomic Distances and Ligand Orientations in the Iminolithium Hexamers [LiNC(Ph)Bu^t]₆ and [LiNC(Ph)NMe₂]₆: A Stacked-Ring Approach to These and Related Oligomeric Organolithium System. *Chem. Commun.* **1986**, No. 4, 295–297. <https://doi.org/10.1039/C39860000295>.
- (2) Prescher, C.; McCammon, C.; Dubrovinsky, L. MossA: A Program for Analyzing Energy-Domain Mössbauer Spectra from Conventional and Synchrotron Sources. *J. Appl. Crystallogr.* **2012**, *45*, 329–331. <https://doi.org/10.1107/S0021889812004979>.
- (3) Bain, G. A.; Berry, J. F. Diamagnetic Corrections and Pascal's Constants. *J. Chem. Ed.* **2008**, *85*, 532–536. <https://doi.org/10.1021/ED085P532>.
- (4) Hertler, P. R.; Lewis, R. A.; Wu, G.; Hayton, T. W. Measuring Metal–Metal Communication in a Series of Ketimide-Bridged [Fe₂]⁶⁺ Complexes. *Inorg. Chem.* **2023**, *62*, 11829–11836. <https://doi.org/10.1021/acs.inorgchem.3c01109>.
- (5) Mansoor Al Sarraf, A. A.; H. Alsultany, F.; H. Mahmoud, Z.; S. Shafik, S.; I. Al Mashhadani, Z.; Sajjadi, A. Magnetic Nanoparticles Supported Zinc (II) Complex (Fe₃O₄@SiO₂-Imine/Thio-Zn(OAc)₂): A Green and Efficient Magnetically Reusable Zinc Nanocatalyst for Synthesis of Nitriles via Cyanation of Aryl Iodides. *Synth. Commun.* **2022**, *52*, 1245–1253. <https://doi.org/10.1080/00397911.2022.2079992>.
- (6) de Haan, J. W.; van de Ven, L. J. M.; Wilson, A. R. N.; van der Hout-Lodder, A. E.; Altona, C.; Faber, D. H. Temperature Effects on ¹³C N.M.R. Chemical Shifts of Normal Alkanes and Some Linear and Branched 1-Alkenes. *Org. Magn. Reson.* **1976**, *8*, 477–482. <https://doi.org/10.1002/mrc.1270080909>.
- (7) Jordan, A. Y.; Meyer, T. Y. C–H Activation of Pendant Alkoxides by Tungsten Imide Complexes. *J. Organomet. Chem.* **1999**, *591*, 104–113. [https://doi.org/10.1016/S0022-328X\(99\)00423-4](https://doi.org/10.1016/S0022-328X(99)00423-4).
- (8) Rodríguez, R. I.; Mollari, L.; Alemán, J. Light-Driven Enantioselective Synthesis of Pyrroline Derivatives by a Radical/Polar Cascade Reaction. *Angew. Chem. Int. Ed.* **2021**, *60*, 4555–4560. <https://doi.org/10.1002/anie.202013020>.
- (9) Navrátil, R.; Tarábek, J.; Linhart, I.; Martinů, T. Radical and Nitrenoid Reactivity of 3-Halo-3-Phenyldiazirines. *Org. Lett.* **2016**, *18*, 3734–3737. <https://doi.org/10.1021/acs.orglett.6b01753>.
- (10) Shibata, S.; Masui, Y.; Onaka, M. Efficient Solvent-Free Synthesis of *N*-Unsubstituted Ketimines from Ketones and Ammonia on Porous Solid Acids. *Tetrahedron Lett.* **2021**, *67*, 152840. <https://doi.org/10.1016/j.tetlet.2021.152840>.
- (11) SMART Apex II., 2005.
- (12) SAINT Software User's Guide, 2005.
- (13) Sheldrick, G. M. SADABS, 2005.
- (14) SHELXTL PC, 2005.
- (15) Frisch, M. J.; Trucks, G. W.; Schlegel, H. B.; Scuseria, G. E.; Robb, M. A.; Cheeseman, J. R.; Scalmani, G.; Barone, V.; Petersson, G. A.; Nakatsuji, H.; Li, X.; Caricato, M.; Marenich, A. V.; Bloino, J.; Janesko, B. G.; Gomperts, R.; Mennucci, B.; Hratchian, H. P.; Ortiz, J. V.; Izmaylov, A. F.; Sonnenberg, J. L.; Williams-Young, D.; Ding, F.; Lipparini, F.; Egidi, F.;

- Goings, J.; Peng, B.; Petrone, A.; Henderson, T.; Ranasinghe, D.; Zakrzewski, V. G.; Gao, J.; Rega, N.; Zheng, G.; Liang, W.; Hada, M.; Ehara, M.; Toyota, K.; Fukuda, R.; Ishida, M.; Nakajima, T.; Honda, Y.; Hasegawa, J.; Kitao, O.; Nakai, H.; Vreven, T.; Throssel, K.; Montgomery, J. A. Jr.; Peralta, J. E.; Ogliaro, F.; Bearpark, M. J.; Heyd, J. J.; Brothers, E. N.; Kudin, K. N.; Staroverov, V. N.; Keith, T. A.; Kobayashi, R.; Normand, J.; Raghavachari, K.; Rendell, A. P.; Burant, J. C.; Iyengar, S. S.; Tomasi, J.; Cossi, M.; Millam, J. M.; Klene, M.; Adamo, C.; Cammi, R.; Ochterski, J. W.; Martin, R. L.; Morokuma, K.; Farkas, O.; Foresman, J. B.; Fox, D. J. *Gaussian 16*, Revision A.03, 2016. https://gaussian.com/citation_a03/ (accessed 2024-05-06).
- (16) Becke, A. D. A New Mixing of Hartree–Fock and Local Density-functional Theories. *J. Chem. Phys.* **1993**, *98*, 1372–1377. <https://doi.org/10.1063/1.464304>.
- (17) Lee, C.; Yang, W.; Parr, R. G. Development of the Colle-Salvetti Correlation-Energy Formula into a Functional of the Electron Density. *Phys. Rev. B* **1988**, *37*, 785–789. <https://doi.org/10.1103/PhysRevB.37.785>.
- (18) Tao, J.; Perdew, J. P.; Staroverov, V. N.; Scuseria, G. E. Climbing the Density Functional Ladder: Nonempirical Meta–Generalized Gradient Approximation Designed for Molecules and Solids. *Phys. Rev. Lett.* **2003**, *91*, 146401. <https://doi.org/10.1103/PhysRevLett.91.146401>.
- (19) Staroverov, V. N.; Scuseria, G. E.; Tao, J.; Perdew, J. P. Comparative Assessment of a New Nonempirical Density Functional: Molecules and Hydrogen-Bonded Complexes. *J. Chem. Phys.* **2003**, *119*, 12129–12137. <https://doi.org/10.1063/1.1626543>.
- (20) Staroverov, V. N.; Scuseria, G. E.; Tao, J.; Perdew, J. P. Erratum: “Comparative Assessment of a New Nonempirical Density Functional: Molecules and Hydrogen-Bonded Complexes” [*J. Chem. Phys.* *119*, 12129 (2003)]. *J. Chem. Phys.* **2004**, *121*, 11507. <https://doi.org/10.1063/1.1795692>.
- (21) Zhao, Y.; Truhlar, D. G. A New Local Density Functional for Main-Group Thermochemistry, Transition Metal Bonding, Thermochemical Kinetics, and Noncovalent Interactions. *J. Chem. Phys.* **2006**, *125*, 194101. <https://doi.org/10.1063/1.2370993>.
- (22) Grimme, S.; Ehrlich, S.; Goerigk, L. Effect of the Damping Function in Dispersion Corrected Density Functional Theory. *J. Comput. Chem.* **2011**, *32*, 1456–1465. <https://doi.org/10.1002/jcc.21759>.
- (23) Weigend, F.; Ahlrichs, R. Balanced Basis Sets of Split Valence, Triple Zeta Valence and Quadruple Zeta Valence Quality for H to Rn: Design and Assessment of Accuracy. *Phys. Chem. Chem. Phys.* **2005**, *7*, 3297–3305. <https://doi.org/10.1039/B508541A>.
- (24) Li Manni, G.; Fdez. Galván, I.; Alavi, A.; Aleotti, F.; Aquilante, F.; Autschbach, J.; Avagliano, D.; Baiardi, A.; Bao, J. J.; Battaglia, S.; Birnoschi, L.; Blanco-González, A.; Bokarev, S. I.; Broer, R.; Cacciari, R.; Calio, P. B.; Carlson, R. K.; Carvalho Couto, R.; Cerdán, L.; Chibotaru, L. F.; Chilton, N. F.; Church, J. R.; Conti, I.; Coriani, S.; Cuéllar-Zuquin, J.; Daoud, R. E.; Dattani, N.; Decleva, P.; de Graaf, C.; Delcey, M. G.; De Vico, L.; Dobrautz, W.; Dong, S. S.; Feng, R.; Ferré, N.; Filatov(Gulak), M.; Gagliardi, L.; Garavelli, M.; González, L.; Guan, Y.; Guo, M.; Hennefarth, M. R.; Hermes, M. R.; Hoyer, C. E.; Huix-Rotllant, M.; Jaiswal, V. K.; Kaiser, A.; Kaliakin, D. S.; Khamesian, M.; King, D. S.; Kochetov, V.; Krośnicki, M.; Kumar, A. A.; Larsson, E. D.; Lehtola, S.; Lepetit, M.-B.; Lischka, H.; López Ríos, P.; Lundberg, M.; Ma, D.; Mai, S.; Marquetand, P.; Merritt, I. C. D.; Montorsi, F.; Mörchen, M.; Nenov, A.;

- Nguyen, V. H. A.; Nishimoto, Y.; Oakley, M. S.; Olivucci, M.; Opper, M.; Padula, D.; Pandharkar, R.; Phung, Q. M.; Plasser, F.; Raggi, G.; Rebolini, E.; Reiher, M.; Rivalta, I.; Roca-Sanjuán, D.; Romig, T.; Safari, A. A.; Sánchez-Mansilla, A.; Sand, A. M.; Schapiro, I.; Scott, T. R.; Segarra-Martí, J.; Segatta, F.; Sergentu, D.-C.; Sharma, P.; Shepard, R.; Shu, Y.; Staab, J. K.; Straatsma, T. P.; Sørensen, L. K.; Tenorio, B. N. C.; Truhlar, D. G.; Ungur, L.; Vacher, M.; Veryazov, V.; Voß, T. A.; Weser, O.; Wu, D.; Yang, X.; Yarkony, D.; Zhou, C.; Zobel, J. P.; Lindh, R. The OpenMolcas Web: A Community-Driven Approach to Advancing Computational Chemistry. *J. Chem. Theory Comput.* **2023**, *19*, 6933–6991. <https://doi.org/10.1021/acs.jctc.3c00182>.
- (25) Roos, B. O. The Complete Active Space Self-Consistent Field Method and Its Applications in Electronic Structure Calculations. In *Advances in Chemical Physics*; John Wiley & Sons, Ltd, 1987; pp 399–445. <https://doi.org/10.1002/9780470142943.ch7>.
- (26) Andersson, K.; Malmqvist, P.; Roos, B. O. Second-order Perturbation Theory with a Complete Active Space Self-consistent Field Reference Function. *J. Chem. Phys.* **1992**, *96*, 1218–1226. <https://doi.org/10.1063/1.462209>.
- (27) Li Manni, G.; Carlson, R. K.; Luo, S.; Ma, D.; Olsen, J.; Truhlar, D. G.; Gagliardi, L. Multiconfiguration Pair-Density Functional Theory. *J. Chem. Theory Comput.* **2014**, *10*, 3669–3680. <https://doi.org/10.1021/ct500483t>.
- (28) Pandharkar, R.; Hermes, M. R.; Truhlar, D. G.; Gagliardi, L. A New Mixing of Nonlocal Exchange and Nonlocal Correlation with Multiconfiguration Pair-Density Functional Theory. *J. Phys. Chem. Lett.* **2020**, *11*, 10158–10163. <https://doi.org/10.1021/acs.jpcclett.0c02956>.
- (29) Pierloot, K.; Dumez, B.; Widmark, P.-O.; Roos, B. O. Density Matrix Averaged Atomic Natural Orbital (ANO) Basis Sets for Correlated Molecular Wave Functions. *Theoret. Chim. Acta* **1995**, *90*, 87–114. <https://doi.org/10.1007/BF01113842>.
- (30) Peng, D.; Reiher, M. Exact Decoupling of the Relativistic Fock Operator. *Theor. Chem. Acc.* **2012**, *131*, 1081. <https://doi.org/10.1007/s00214-011-1081-y>.
- (31) Aquilante, F.; Pedersen, T. B.; Lindh, R. Low-Cost Evaluation of the Exchange Fock Matrix from Cholesky and Density Fitting Representations of the Electron Repulsion Integrals. *J. Chem. Phys.* **2007**, *126*, 194106. <https://doi.org/10.1063/1.2736701>.
- (32) Roos, B. O.; Malmqvist, P.-Å. Relativistic Quantum Chemistry: The Multiconfigurational Approach. *Phys. Chem. Chem. Phys.* **2004**, *6*, 2919–2927. <https://doi.org/10.1039/B401472N>.
- (33) Heß, B. A.; Marian, C. M.; Wahlgren, U.; Gropen, O. A Mean-Field Spin-Orbit Method Applicable to Correlated Wavefunctions. *Chem. Phys. Lett.* **1996**, *251*, 365–371. [https://doi.org/10.1016/0009-2614\(96\)00119-4](https://doi.org/10.1016/0009-2614(96)00119-4).
- (34) Malmqvist, P. Å.; Roos, B. O.; Schimmelpfennig, B. The Restricted Active Space (RAS) State Interaction Approach with Spin–Orbit Coupling. *Chem. Phys. Lett.* **2002**, *357*, 230–240. [https://doi.org/10.1016/S0009-2614\(02\)00498-0](https://doi.org/10.1016/S0009-2614(02)00498-0).
- (35) Zhou, C.; Wu, D.; Gagliardi, L.; Truhlar, D. G. Calculation of the Zeeman Effect for Transition-Metal Complexes by Multiconfiguration Pair-Density Functional Theory. *J. Chem. Theory Comput.* **2021**, *17*, 5050–5063. <https://doi.org/10.1021/acs.jctc.1c00208>.
- (36) Chibotaru, L.; Ungur, L. The Computer Programs SINGLE_ANISO and POLY_ANISO, 2006.